

On Seismic Gradiometric Wave Equation Inversion for Density

Marthe Faber* and Andrew Curtis

University of Edinburgh, School of Geosciences, Edinburgh, UK

E-mails: M.Faber@sms.ed.ac.uk (M.Faber), Andrew.Curtis@ed.ac.uk (A.Curtis)

Abstract

Material density remains poorly constrained in seismic imaging problems, yet knowledge of density would provide important insight into physical material properties for the interpretation of subsurface structures. We test ambient noise wavefield sensitivities to subsurface density contrasts through spatial and temporal wavefield gradients via Wave Equation Inversion (WEI), a form of seismic gradiometry. Synthetic results for 3D acoustic media suggest that it is possible to estimate relative density structure with WEI by using a full acoustic formulation for wave propagation and gradiometry. We show that imposing a constant density assumption on the medium can be detrimental to subsurface velocity images, whereas the full acoustic formulation assuming variable density improves our knowledge of both material properties. It allows us to estimate density as an additional material parameter, as well as to improve phase velocity estimates by accounting for approximations to the density structure. In 3D elastic media, severe approximations in governing wave physics are necessary in order to invert for density using only an array of receivers on the free surface. It is then not straightforward to isolate the comparatively weak density signal from the influence of phase velocity using gradiometric WEI. However, by using receivers both at the surface and in the shallow subsurface we show that it is possible to estimate density using fully elastic volumetric WEI.

Key words: Seismic gradiometry; Wave Equation Inversion; Density; Full acoustic approximation; Ambient noise

*Corresponding author.

1 Introduction

Dynamic processes in the Earth’s shallow subsurface (top few 100 m) in which rocks, soil, atmospheric gases and meteoric water interact are seldom well characterised and understood (Parsekian et al., 2015, Riebe et al., 2017). It is of interest for environmental and resource applications to better characterize these chemical and mechanical processes using information about the heterogeneity in properties of the near-surface, so-called critical zone (Anderson et al., 2007). In critical zone studies, bulk density is an important physical property as an indicator for soil quality and compaction (Suuster et al., 2011). Lateral density variations can reveal information about changes in porosity, fracture distribution and soil weathering (Flinchum et al., 2022). Density is used to inform studies of root growth (Brimhall et al., 1992; Dexter, 2004), water movement and retention (Huang et al., 2011; Flinchum et al., 2018), as well as carbon and nutrient content in soil layers (Nanko et al., 2014). It is therefore of significant interest to be able to estimate near-surface density.

Direct density measurements can be obtained via auger samples or Geoprobe coring (Holbrook et al., 2014). Given that obtaining in-situ measurements of bulk density at any significant depth is time-intensive and expensive, it may be preferable to estimate density indirectly. So-called pedotransfer functions are used to predict bulk density based on regression models from soil measurement archives for the very shallow subsurface (< 1 m) (Suuster et al., 2011). However, due to the sparsity of borehole samples from deep soil layers, few studies are able to estimate bulk density for deeper targets (Qiao et al., 2019). Well logs can be used to gain insight on bulk density and to infer porosity of the logged near-surface interval (Fanchi, 2010, Holbrook et al., 2019), but remain invasive, localized and again expensive sources of information.

Geophysical methods complement direct observations. They allow larger and deeper subsurface volumes to be investigated, and temporal changes in properties to be monitored (Parsekian et al., 2015). Microgravity surveys are directly sensitive to density anomalies and are commonly used for environmental studies of the subsurface, e.g., to localize subsurface voids (Tuckwell et al., 2008) or for groundwater monitoring (Piccolroaz et al., 2015). However, this data type is strongly impacted by microseismic noise which might overshadow small signals related to mass distributions in the near surface (Boddice et al., 2022). Signals from density variations in the near surface soil (top 5 m) for example have been shown to be too weak to be detected by current gravity instrumentation, leading to lateral variations being obscured by the influence of deeper anomalies (Boddice et al., 2019). Furthermore, inversion procedures for subsurface density on the basis of gravity data alone are inherently ill-posed (Blom et al., 2017). To reduce the non-uniqueness in solutions, gravity measurements must be used in conjunction with other data types such as geological prior knowledge,

well-log densities or seismic data to produce realistic density maps (Nabighian et al., 2005).

Seismic imaging provides another non-invasive alternative to investigate the critical zone. Active methods such as seismic refraction tomography (Befus et al., 2011; Nielson et al., 2021; Flinchum et al., 2022) and multi-channel surface wave analysis (Handoyo et al., 2022, Trichandi et al., 2022) are popular methods for imaging the near-surface. Seismic monitoring of dynamic processes may be achieved using omnipresent ambient seismic noise, a natural source of energy in the Earth (Curtis et al., 2006; Obermann et al., 2015; Nakata et al., 2019), and dense arrays of seismometers may be used to provide a repeatable data source with high spatial resolution. Ambient noise seismology has thus allowed velocity changes over time to be monitored in the critical zone (James et al., 2019; Oakley et al., 2021).

Seismic methods usually focus on the retrieval of seismic velocities only, and are unable to isolate the signal corresponding to subsurface density unambiguously. Density values are often inferred via empirical relationships from the speed of P body-waves (e.g. Gardner et al., 1974), and estimating density as a seismic observable still remains a challenge. Body wave traveltime tomography exhibits an inherent insensitivity to density changes: body wave scattering caused by a density contrast characteristically propagates backwards rather than forwards, and so to first order does not interact with the forward propagating incident wave whose traveltime is measured (Fichtner, 2010). Surface waves, however, can be represented as an infinite sum of reflections and conversions between the free surface and subsurface interfaces, where the reflection coefficients depend on the density in the vicinity of the surface; this in turn affects the phase velocities of dispersive surface waves. Their frequency dependent arrival times are therefore sensitive to density variations in the subsurface, but the sensitivity is oscillatory with depth and can cancel destructively (Takeuchi and Saito, 1972).

In the context of global seismology, where density plays an important role in explaining mantle dynamics, several studies have been conducted to invert for density from surface wave data. Nolet et al. (1977) showed that Rayleigh wave dispersion data are sensitive to the density structure in elastic media, as are normal modes at longer periods (Tanimoto, 1991). It is however usually considered too challenging to estimate density in most elastic media using surface wave dispersion alone because the sensitivity is relatively weak compared to sensitivity to seismic velocity structure (Muyzert and Snieder, 2000). Due to the poor constraints on density, it has been common practice in surface wave tomography to prescribe a scaling relation between density and shear velocity anomalies (Karato and Karki, 2001) and to invert for velocity only. From seismological research, however, we know that anti-correlation of density and seismic velocity are observed: Resovsky and

Trampert (2003) show that the long period seismic data clearly favour density perturbations that are poorly or negatively correlated with velocity heterogeneity and have larger amplitudes. The uniform scaling of velocity and density in tomography arises under the assumption that density variations are purely thermal; this is not accurate for density variations related to compositional heterogeneities or liquid/gas inclusions (Płonka et al., 2016). Therefore, independent knowledge of density is important in order to discriminate between compositional and thermal heterogeneities (Trampert et al., 2004; Mosca et al., 2012). Additional observables such as horizontal to vertical ratios (H/V) of surface waves can provide further constraints on density (Lin et al., 2012) but still show strong trade-offs with elastic parameters and velocity.

Variations in density also generally have a smaller effect on the full, recorded seismic waveforms than variations in seismic velocity (Blom et al., 2017), and are subject to strong trade-offs with velocity which depend on the scattering angle of the wave (Luo and Wu, 2018). Nevertheless, Płonka et al. (2016) show that amplitude variations caused by realistic crustal density variations have measurable effects on seismograms. Density effects are mainly visible as an amplitude change, but also cause the waveform shape to be altered especially in the scattered wave train (Blom et al., 2017; Yuan et al., 2015). Hence, seismic methods that investigate the full seismic waveform such as full waveform tomography (Płonka et al., 2016; Blom et al., 2017; Blom et al., 2020) which includes both phases and amplitudes of body, surface and scattered waves, show promise to glean further constraints on subsurface density. However, in elastic multi-parameter full waveform inversion (FWI), the highest ambiguity is attached to density regardless of the employed model parametrizations (Köhn et al., 2012), and it is difficult to reconstruct density from full waveform inversion even using the dense data sets available in industrial exploration geophysics (Virieux and Operto, 2009). Choi et al. (2008) successfully estimated density from 2D elastic Marmousi models, but only using a low and narrow frequency band around 0.125 Hz. W. Pan et al. (2018) observed that S-wave velocity perturbations strongly contaminate density structure which can result in highly uncertain density estimates. Jeong et al. (2012) reports improvement in density recovery by implementing a 2-step algorithm that estimates Lamé parameters with fixed density in a first step, then velocity and density are estimated in a subsequent step that varies the number of free parameters in an iterative scheme. Subsurface density of the ocean floor can be reliably estimated from real hydrophone data on the basis of a joint visco-acoustic FWI (Prioux et al., 2013; Operto and Miniussi, 2018) and can be used as a background model to inform and reduce free parameters in elastic FWI. However, the performance of linearised FWI algorithms depends on a well informed starting model (Virieux and Operto, 2009; Vantassel et al., 2022).

Density affects the seismic wavefield mainly through reflection/backscattering. Hence, the strongest sensi-

tivity of seismic waves is to spatial density contrasts or gradients (Blom et al., 2020). Hooke’s law relates stress to strain, and strain is created by spatial wavefield gradients. In turn, stress can be related to density using Newton’s second law, to form a so-called wave equation. This sparked interest in constraining density contrasts by deploying methods that are directly sensitive to amplitude changes in the wavefield gradients. Dense seismic arrays lend themselves well to the calculation of wavefield gradients using finite-difference methods.

A class of imaging techniques now termed seismic gradiometry (Curtis and Robertsson, 2002; Langston, 2007b; Langston, 2007c; De Ridder and Biondi, 2015) calculate temporal and spatial gradients of incoming waves or wavefields using dense array measurements to estimate physical subsurface parameters. A review of the theoretical background and applications of the wave gradiometry method can be found in Liang et al. (2023). One such method called wave equation inversion (WEI - Curtis and Robertsson, 2002) substitutes the calculated gradients directly into the governing equation for wave propagation and provides estimates of local material properties via standard linear inversion techniques. By deploying a 3D seismic array geometry with receivers recording all three components (3-C) of the wavefield, gradients can be estimated both horizontally at the surface and with respect to depth (Fig. 1a). WEI can then be performed on the full elastic wave equation to estimate effective P and S wave velocities at the free surface. In an isotropic, locally homogeneous Earth, full elastic WEI is valid for any incoming wavefield; it thus has the advantage of being directly applicable to ambient seismic wavefields, but exhibits a high sensitivity to receiver positioning and orientation (Muijs et al., 2002; Vossen et al., 2004). A second type of gradiometric research assumes a particular form or ansatz for the arriving wavefield (e.g., a single plane or spherically spreading wave (Fig. 1b), and estimates parameters that describe the geometrical spreading and horizontal slowness (Langston, 2007a; Langston, 2007c). The method was applied for example as a new data processing technique for regional array seismology (Liang and Langston, 2009; Liu and Holt, 2015) and used to image the lunar near-surface structure (Sollberger et al., 2016). The method performs well for noiseless single source data, but gradiometry results based on the plane-wave assumption are highly sensitive to uncorrelated noise and to interference from other arriving waves (Langston, 2007b). In order to use such methods in cases of unclassified wave type arrivals or ambient seismic noise, where two or more waves of similar amplitude and frequency are interfering, a statistical routine to identify individual interference-free events needs to be applied in advance (Edme and Yuan, 2016). A novel ‘fingerprinting’ technique based on 6C receiver measurements, which contain both translational and rotational ground motion, now allows to rapidly classify the wave types of seismic phases and extract individual arrivals from interfering wavefields using machine learning methods (Sollberger et al., 2023).

157 In the case of an ambient seismic noise field, it is commonly assumed that surface waves are the dominating
 158 type of wave propagation. To capture the character of 2D surface wave propagation, it is sufficient to record
 159 the wavefield with a dense receiver array at the Earth's surface (Fig. 1c). This relaxes the condition on the
 160 field acquisition geometry compared to volumetric gradiometry which requires a 3D array (Fig. 1a), while still
 161 allowing a wavefield comprising a superposition of plane waves arriving from different angles to be considered
 162 instead of only individual plane waves (Fig. 1b). De Ridder and Biondi (2015) first approximated surface
 163 wave WEI on the basis of the 2D Helmholtz wave equation which describes the propagation of surface waves
 164 at frequency dependant phase velocities (Wielandt, 1993; Aki and Richards, 2002). The method showed that
 165 phase velocity maps from the vertical component of ambient noise data at 0.7 Hz were comparable to results
 166 from interferometric cross-correlations, thus validating the method. The method has since been extended
 167 to provide information on both isotropic and anisotropic local medium properties (De Ridder and Curtis,
 168 2017), and to near-real time applications (Cao et al., 2020).

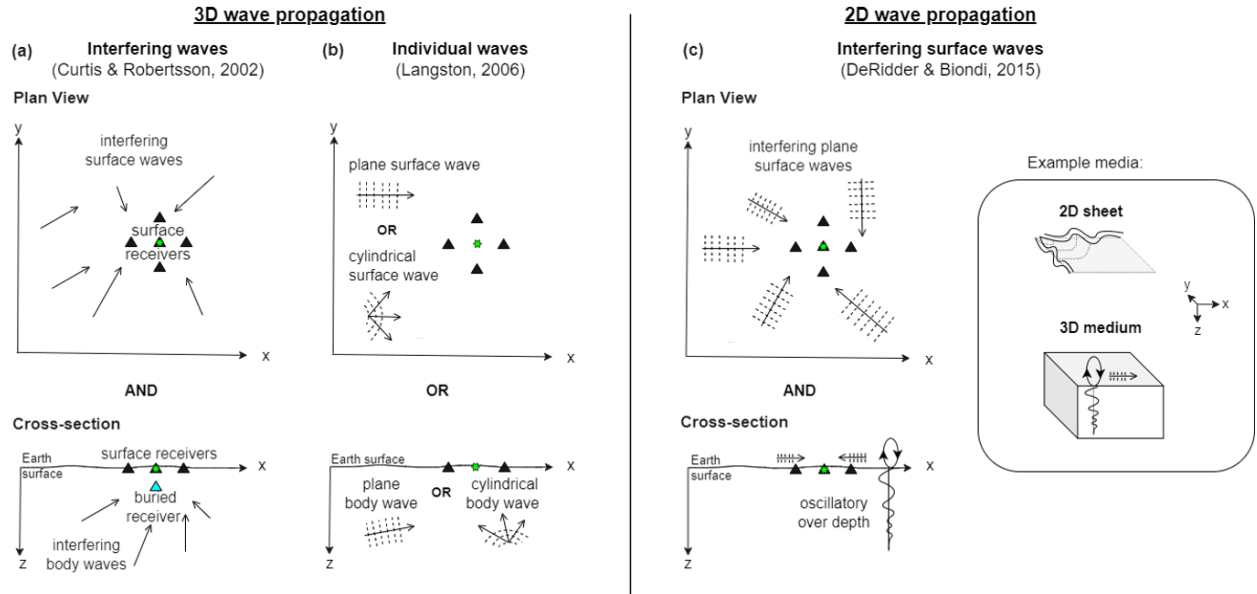


Figure 1: Schematic of acquisition geometries and physical assumptions made for different gradiometry types in plan view and cross-section view. Receivers are denoted by triangles and the configurations requiring the minimum number of receivers are shown to estimate gradients via classical finite difference around the central point (green star) with receivers recording translational motion. (a) The left column shows principles of volumetric wavefield gradiometry as proposed by (Curtis and Robertsson, 2002): with a 3D receiver acquisition, second horizontal and vertical wavefield derivatives are approximated at a central point. To calculate derivatives in x-, y- and z-direction, 3-component (3C) receivers are necessary. Arrows denote interfering waves coming from all directions and angles; all wave types can be included in the wavefield e.g., surface waves, body waves, scattered waves, etc. (b) Middle column shows gradiometry for non-interfering waves as proposed by (Langston, 2007b). Individual plane or cylindrical waves can arrive from any direction at the receiver array. Receivers are used to estimate first horizontal derivatives of the wave field quantity; the central point does not require a recording. Receivers can be (1C) or (3C) depending on which wave type is analysed. Rotational sensors at the free surface allow for direct measurement of first derivatives (Schmelzbach et al., 2018; Sollberger et al., 2020). (c) Right column shows principles of surface wave gradiometry as proposed by (De Ridder and Biondi, 2015) where second order horizontal wavefield derivatives are approximated. This gradiometry type assumes a wavefield composed of interfering surface plane waves in a 3D medium, or Lamb waves in a 2D sheet (inset).

The latter applications of surface wave WEI are based on the assumption that Rayleigh waves are the dominant wave type and that the 2D scalar Helmholtz wave equation describes the recorded wavefield adequately (De Ridder and Biondi, 2015; Cao et al., 2020). This is a significant approximation for seismic waves because the Helmholtz equation fails to describe general elastic wavefield dynamics. Since ambient noise recordings contain all kinds of interfering elastic wave types (such as surface waves themselves), the accuracy of subsurface material property estimates may be compromised. Nevertheless, Shaiban et al. (2022) used a synthetic 2D elastic ambient noise wavefield to show that the correct local dispersion curves for a layered, laterally heterogeneous model could be estimated from the relationship between spatial and temporal gradients in the Helmholtz equation.

Surface wave WEI has been shown to require only a few minutes of ambient seismic noise recordings and rapid data processing after acquisition to produce useful phase velocity maps for the near-surface (at frequencies between 18 Hz to 24 Hz), and so shows promise for efficient field deployment and near-real time monitoring purposes for the shallow subsurface (Cao et al., 2020). By estimating phase velocity maps for narrow band-pass filtered wavefields over a broad frequency range (depending on the ambient noise spectrum), the latter authors showed that 3D images of a layered subsurface can be produced via inversion of local surface-wave dispersion curves for S-wave velocity (V_s) structure. 2D shear-velocity maps for several depth levels up to 50 m were obtained in a matter of seconds from the dispersion curve through depth inversion performed by mixture-density neural networks (MDN). However, the quality of the 3D shear velocity models are not only dependant on the accuracy of the phase velocity data but also on the impact of density in the inversion process (Ivanov et al., 2016). Dispersion-curve inversion for V_s generally uses predefined values for compressional-wave velocity (V_p) and density because their sensitivities to the phase velocity are much smaller than that of the S-wave velocity (Foti et al., 2018; L. Pan et al., 2019; Wu et al., 2020). Such a-priori information on V_p is commonly obtained from other measurements and density is often assumed constant (e.g. Cao et al., 2020) or inferred from empirical relationships with compressional wave speed. Unfortunately, vertical density variations have been shown to affect the inverted V_s results, and the use of an inaccurate density background model can lead to false structures and overestimations in the V_s result (Ivanov et al., 2016). Expanding surface wave WEI to estimate the density structure of the subsurface and to quantify the effect of density gradients on the phase velocity estimates could therefore improve V_s models and seismic interpretation based on gradiometric methods.

In this study we investigate whether it is possible to estimate subsurface density on the basis of gradiometric surface wave WEI using ambient seismic noise. Both the accuracy in wave amplitude and shape are impor-

tant considerations in gradiometric methods, and density heterogeneities were found to have an influence on both (Płonka et al., 2016; Blom et al., 2017). Hence, we expect to have sensitivity to the effect of density contrasts by using data that record variations in wavefield amplitudes and phases.

In the Helmholtz formulation, which has been used in previous surface wave WEI studies, the wave equation does not exhibit an explicit sensitivity to density. In elastic media, the scalar Helmholtz wave equation is valid for surface waves only in laterally homogeneous medium. In a realistic scenario, the subsurface is heterogeneous with density varying both laterally and with depth. This implies that the Helmholtz wave equation is not a valid description for surface wave propagation (Friederich et al., 2000) and is likely to influence the accuracy of phase velocity estimates made via 2D scalar WEI. Seismic surface waves are however commonly approximated by acoustic waves, by assuming that the wavefield is purely dilatational and is dominated by pressure wave propagation. The acoustic approximations neglects mode conversions and the directivity of scattering from a point heterogeneity (Friederich et al., 2000), simplifying the mathematical model of wave propagation considerably.

The scalar Helmholtz wave equation more accurately describes waves in acoustic media than in elastic media. In fact in the acoustic case, the main simplification made in the derivation of the conventional scalar wave equation is that density is assumed to be constant across the local receiver array. To describe a more complex, physically more realistic medium, a variable density assumption can be made, which allows the acoustic medium to be described by a so-called full acoustic wave equation. The full acoustic wave equation was initially derived by Bergmann (1946) to define conditions under which density gradients in the atmosphere and large bodies of water should not be neglected in the governing wave equation formulation of sound pressure. The formulation of the full acoustic wave equation considered in that work assumes that gravity effects are negligible, and allows for density changes caused by either temperature gradients or changes in chemical composition of the material (Bergmann, 1946).

In this paper we analyse wavefield sensitivities to subsurface density contrasts via WEI of the full-acoustic wave equation where density is treated as a variable. We expect the full acoustic formulation may allow us to analyse the role of density independently from wave speed. To test this hypothesis, we initially consider waves propagating through an acoustic medium so that the physics of the used wave equation are consistent with the physics of the medium. We show that it is possible to invert for density on the basis of full acoustic WEI and compare the effect of using the Helmholtz and full acoustic equation on phase velocity results in 3D acoustic media. We then analyse whether the procedure is applicable to elastic media despite the con-

comitant severe approximations to the complex elastic wavefield physics. In elastic media, particle velocity is the natural wavefield observable rather than pressure, but we show that measuring pressure is necessary in order to relate the full acoustic wave equation approximation to the elastic case and to formulate an inverse algorithm that is explicitly sensitive to density. We then investigate whether volumetric gradiometry better lends itself to invert for density using the physically more representative full elastic wave equation at the free surface. By expressing the full elastic wave equation both in terms of pressure and displacement at the free surface we establish that a direct sensitivity to density exists and that density can be estimated.

2 Wave Theoretical Background

Density plays a different role in elastic and acoustic media. To illustrate, we compare the derivations of the respective governing wave equations from Newton's 2nd Law

$$\nabla \cdot \sigma + \mathbf{f} = \rho \partial_t^2 \mathbf{u} \quad (1)$$

where $\sigma = \sigma_{kl}$ is the stress tensor assuming k and l to range from 1 to 3 (for the x , y and z directions), ρ is subsurface density, $\mathbf{f} = [f_x, f_y, f_z]^T$ is the distribution of applied body forces, $\mathbf{u} = [u_x, u_y, u_z]^T$ the observed wave field quantity of displacement or particle velocity, and $\nabla = [\partial_x, \partial_y, \partial_z]^T$ in three dimensional media. It is well known that in isotropic elastic media and small displacements, Hooke's law allows stress to be expressed in terms of the strain tensor ϵ (where element $\epsilon_{xy} = \partial_x u_y + \partial_y u_x$ and similarly for other elements) and the Lamé parameters λ and μ . This relationship can then be substituted in equation (1). Similarly for acoustic media, however the equations are then simpler because the shear modulus $\mu = 0$:

$$\nabla \cdot (\lambda \operatorname{tr}(\epsilon) \mathbf{I} + 2\mu\epsilon) + \mathbf{f} = \rho \partial_t^2 \mathbf{u} \quad \text{in elastic media} \quad (2a)$$

$$\nabla \cdot (\lambda \operatorname{tr}(\epsilon) \mathbf{I}) + \mathbf{f} = \rho \partial_t^2 \mathbf{u} \quad \text{in acoustic media} \quad (2b)$$

where $\operatorname{tr}()$ is the trace operator. By substituting expressions for elements of ϵ into equations (2a) and (2b) we obtain the familiar 3D elastic wave equation for isotropic, locally homogeneous media, and a description of pressure wave propagation in terms of the wave field quantity \mathbf{u} , respectively:

$$\frac{(\lambda + 2\mu)}{\rho} [\nabla(\nabla \cdot \mathbf{u})] - \frac{\mu}{\rho} [\nabla \times (\nabla \times \mathbf{u})] + \frac{\mathbf{f}}{\rho} = \partial_t^2 \mathbf{u} \quad \text{in elastic media} \quad (3a)$$

$$\frac{\lambda}{\rho} [\nabla(\nabla \cdot \mathbf{u})] + \frac{\mathbf{f}}{\rho} = \partial_t^2 \mathbf{u} \quad \text{in acoustic media} \quad (3b)$$

In this paper we focus on the case in which we would like to use ambient seismic noise, so we assume an absence of strong local sources in the area of wavefield recording and henceforth omit source term \mathbf{f} . In acoustic media, the first Lamé parameter λ is the acoustic bulk modulus K_a , whereas the bulk modulus in elastic media is $K_e = \lambda + \frac{2}{3}\mu$. In elastic media, density is expressed only in combination with the Lamé parameters within the terms equating to P-wave velocity $v_{P,e} = \sqrt{(\lambda + 2\mu)/\rho}$ and S-wave velocity $v_{S,e} = \sqrt{\mu/\rho}$ respectively in equation (3a), and similarly for acoustic media. This implies that while it may be possible to estimate the velocities from waveform data \mathbf{u} , it will not be possible to discriminate the Lamé parameters from the density since any velocity value can be fit by any density given a suitable choice of λ and μ .

In acoustic media, we often measure pressure P rather than wavefield displacement or particle velocity. The particle velocity field can then be estimated from this measured pressure field (Robertsson and Kragh, 2002; Amundsen et al., 2005). Pressure is directly related to the divergence of the wavefield displacement \mathbf{u} via the equality $P = K_a \nabla \cdot \mathbf{u}$, where K_a is the bulk modulus in acoustic media and $\nabla = [\partial_x, \partial_y, \partial_z]^T$. By applying a divergence operator to both sides of the acoustic wave equation (3b) it is possible to express an explicit sensitivity of measurements of pressure P to density ρ :

$$\nabla \cdot \left(\frac{K_a}{\rho} [\nabla(\nabla \cdot \mathbf{u})] \right) = \nabla \cdot \partial_t^2 \mathbf{u} \quad (4)$$

$$\Rightarrow \quad \rho \nabla \cdot \left(\frac{1}{\rho} \nabla P \right) v_{P,a}^2 = \partial_t^2 P \quad (5)$$

where in equation (5) we have used the definition of P wave velocity in acoustic media $v_{P,a} = \sqrt{K_a/\rho}$. Since density appears separately from P-wave velocity and has a different relationship to the measurable right hand side of equation (5), we expect a potentially distinguishable density signature in seismic waves travelling through heterogeneous media in which the spatial derivative of density on the left is non-zero.

Cance and Capdeville (2015) show how elastic and acoustic wave equations can be related in an isotropic, homogeneous domain for an explosive isotropic source emitting only P-waves. In such a case, the curl of the wavefield is equal to zero ($\nabla \times \mathbf{u} = 0$) and any vector field such as the displacement \mathbf{u} or the particle velocity field $\mathbf{v} = \partial_t \mathbf{u}$ can be derived from a potential Φ (Kaufman et al., 2000). The potential Φ may be chosen as in Cance and Capdeville (2015) to be

$$\mathbf{u} = \frac{1}{\rho} \nabla \Phi \quad (6)$$

where Φ is directly related to acoustic pressure via the relationship $\Phi = -2P_e$ and where the pressure wavefield P_e in elastic media is

$$P_e = -\frac{1}{2}K_a \nabla \cdot \mathbf{u} \quad (7)$$

Substituting equation (6) into equation (3a) yields,

$$\frac{\lambda + 2\mu}{\rho} \nabla \cdot \left[\nabla \cdot \left(\frac{1}{\rho} \nabla \Phi \right) - \frac{1}{\lambda + 2\mu} \partial_t^2 \Phi \right] = 0 \quad (8)$$

$$\nabla \cdot \left(\frac{1}{\rho} \nabla \Phi \right) - \frac{1}{\lambda + 2\mu} \partial_t^2 \Phi = c \quad (9)$$

Since equation (8) holds everywhere and so constant c is independent of position of the recording, and because the wave is absent (has zero energy) at infinity (Kaufman et al., 2000), equation (9) gives the potential equation in elastic media,

$$\rho \nabla \cdot \left(\frac{1}{\rho} \nabla \Phi \right) c_\omega^2 = \partial_t^2 \Phi \quad (10)$$

which is the equation of acoustic wave propagation in elastic media, the elastic equivalent of equation (5) for acoustic media.

290

The above equations show that different seismic observables interact differently with the subsurface: to isolate the effect of density from wave speed in elastic media on the basis of the full acoustic approximation or the elastic wave equation at the free surface, it is necessary to measure pressure instead of particle displacement or velocity (equations 6 to 10) because pressure implicitly includes a power of K_a which changes the form of the respective equations. Classical seismometers only measure particle velocity, from which displacement can be calculated by time integrating the data, whereas elastic pressure is usually not observed on land. The expression for pressure is proportional to the divergence of the displacement (eq. 7) which can be determined from four geophone recordings at the Earth's free surface using gradiometry (Robertsson and Muyzert, 1999; Shapiro et al., 2000; Robertsson and Curtis, 2002). Given that stress is equal to zero across the free surface, the vertical derivative of the wavefield can be expressed in terms of horizontal derivatives. This results in the wavefield divergence taking a modified form that can be written in terms of the Lamé parameters and the horizontal wavefield components only $\nabla \cdot \mathbf{u} = (2\mu/(\lambda + 2\mu)) \nabla_H \cdot \mathbf{u}^H$ where $\nabla_H = [\partial_x, \partial_y]^T$ and $\mathbf{u}^H = [u_x, u_y]^T$ (e.g. Maeda et al., 2016). However, calculating the divergence alone is not sufficient to estimate subsurface density as the density signal is contained in the full pressure measurement (eq. 7).

305

306 Edme et al. (2018) suggest that it is possible to measure pressure directly at the free surface of an elastic
 307 medium with a land hydrophone. The land hydrophone is insensitive to the direction and angle of incoming
 308 waves which makes it predominantly sensitive to pressure fluctuations induced by ground-roll (more specif-
 309 ically, S-to P-conversions generated by upcoming S-waves) due to destructive summation of events at near
 310 vertical incidence angle. At the free surface of the Earth, elastic pressure $P_{e,FS}$ can be written in terms of
 311 displacement in a 2D plane and its horizontal derivatives as (Edme et al., 2018)

$$P_{e,FS} = K_{e,FS} \nabla_H \cdot \mathbf{u}^H \approx 0.37 K_a \nabla_H \cdot \mathbf{u}^H \quad (11)$$

312 where the elastic bulk modulus at the free surface is $K_{e,FS} = 2\rho v_S^2 (1 - 4v_S^2/3v_P^2)$. The elastic pressure at the
 313 free surface can be related to acoustic pressure using $v_P = \sqrt{3}v_S$. The measured pressure thus corresponds
 314 to the volume change caused by the dilatational part of surface wave propagation.

315

316 Acoustic pressure caused purely by P-wave propagation in a non-rotational medium has a similar expression
 317 to elastic pressure at the free surface caused by the dilatational part of surface wave propagation. Surface
 318 waves can only be produced in a medium where rotation exists, and are generated by P- and S- wave in-
 319 teractions upon reflections and scattering at medium heterogeneities. Their propagation is mostly driven
 320 by S-waves which correspond to the purely rotational part of the wavefield. Nevertheless, Rayleigh waves
 321 do exhibit dilatational wave propagation that produces a measurable pressure field at the free surface. The
 322 full acoustic approximation is only valid for elastic P-waves in a homogeneous, isotropic medium, and is
 323 compromised in heterogeneous or anisotropic media due to P-to-S conversions. It thus does not describe a
 324 wave type that depends on body-wave conversions that are predominantly controlled by S-wave motion, even
 325 if only its compressional part is recorded. P-waves and the P component of Rayleigh waves therefore pre-
 326 sumably interact differently with the medium and might exhibit different sensitivities to different subsurface
 327 parameters such as subsurface density. Cance and Capdeville (2015) found that acoustic and elastic pressure
 328 are not the same for rough, heterogeneous media: a good agreement can only be achieved in homogeneous
 329 or weakly heterogeneous, smooth media. This suggests that in a realistic subsurface problem, inverting for
 330 the parameters on the basis of an acoustic approximation might be too approximate an approach to obtain
 331 sufficiently accurate information about elastic subsurface parameters by measuring pressure. We test this in
 332 what follows.

333

334 In elastic media it is not strictly necessary to consider the acoustic approximation in order to isolate density

335 by substituting pressure. If we introduce the free surface conditions

$$\partial_z u_x = -\partial_x u_z \quad (12)$$

$$\partial_z u_y = -\partial_y u_z \quad (13)$$

$$\partial_z u_z = -\frac{v_{P,e}^2 - 2v_{S,e}^2}{v_{P,e}^2} (\partial_x u_x + \partial_y u_y) \quad (14)$$

336 which express the fact that stress across the free surface must be zero, then equation (3a) can be written in
337 a modified form that is valid at the free surface and in the absence of body forces:

$$\partial_z^2 u_x = \frac{\partial_t^2 u_x}{v_{S,e}^2} - (\nabla_H^2 u_x) - 2\left(1 - \frac{v_{S,e}^2}{v_{P,e}^2}\right) \partial_x (\nabla_H \cdot \mathbf{u}^H) \quad (15)$$

$$\partial_z^2 u_y = \frac{\partial_t^2 u_y}{v_{S,e}^2} - (\nabla_H^2 u_y) - 2\left(1 - \frac{v_{S,e}^2}{v_{P,e}^2}\right) \partial_y (\nabla_H \cdot \mathbf{u}^H) \quad (16)$$

$$\partial_z^2 u_z = \frac{\partial_t^2 u_z}{v_{P,e}^2} + \left(1 - 2\frac{v_{S,e}^2}{v_{P,e}^2}\right) \nabla_H^2 u_z \quad (17)$$

338 By using a so-called Lax-Wendroff derivative centering technique (Lax and Wendroff, 1964; Blanch and
339 Robertsson, 1997; Curtis and Robertsson, 2002), the first order vertical derivative can be correctly repre-
340 sented at the free surface by a finite difference approximation to horizontal spatial derivatives. Using a 3D
341 receiver array as proposed in Fig. 1(a) it then becomes possible to approximate all quantities necessary to
342 estimate body wave velocities at the free surface. For example, a new expression can be derived for the
343 vertical displacement component in eq. (17) by using the free-surface condition (14) and the Lax-Wendroff
344 corrected finite difference depth derivative:

$$\partial_t^2 u_z = v_{P,e}^2 A_z(t) - v_{S,e}^2 B_z(t) \quad (18)$$

345 where $A_z(t)$ and $B_z(t)$ are expressions containing finite difference approximations to derivatives of the wave-
346 field

$$A_z(t) = \frac{2}{\Delta z} (\nabla_H \cdot \mathbf{u}^H + [\partial_z u_z]_{fd}) - \nabla_H^2 u_z \quad (19)$$

$$B_z(t) = \frac{4}{\Delta z} (\nabla_H \cdot \mathbf{u}^H) - 2(\nabla_H^2 u_z) \quad (20)$$

347 and where Δz is the distance between the surface and the buried receiver, and $[\partial_z u_z]_{fd}$ is the first order finite
348 difference depth derivative. The derivation of these expressions is described in detail in Curtis and Roberts-
349 son (2002), and herein, we only consider the constraints derived from the vertical displacement component

as they were shown to better constrain body wave velocity estimates than those derived from horizontal components. Furthermore, inhomogeneous terms do not play a role in the vertical component at the free surface, making the expressions valid for any type of elastic medium without approximations (Appendix C).

By using the relation $P = P_{e,FS}/0.37$ from eq. (11), acoustic pressure can be substituted into eq. (19) and (20):

$$A'_z(t) = \frac{2}{\Delta z} \left(\frac{1}{K_a} P + [\partial_z u_z]_{fd} \right) - \nabla_H^2 u_z \quad (21)$$

$$B'_z(t) = \frac{4}{\Delta z} \frac{1}{K_a} P - 2(\nabla_H^2 u_z) \quad (22)$$

Feeding the expressions for $A'_z(t)$ and $B'_z(t)$ into eq. (18) we obtain

$$\partial_t^2 u_z + v_{P,e}^2 \left[-\frac{2}{\Delta z} [\partial_z u_z]_{fd} + \nabla_H^2 u_z \right] - 2v_{S,e}^2 \nabla_H^2 u_z = \frac{1}{\rho} \left[\frac{1}{\Delta z} \left(2 - \frac{4v_{S,e}^2}{v_{P,e}^2} \right) P \right] \quad (23)$$

Displacement measurements are all on the left-hand side and pressure measurements on the right-hand side of equation (23); in order to use this equation to constrain the velocities and density, both displacement and pressure must be measured simultaneously at the free surface. An explicit sensitivity becomes clear from eq. (23) with density connecting the left- and right-hand sides of the equation linearly.

3 Gradiometric Methodology

3.1 Free surface arrays

In previous wavefield gradiometry studies performed with data from 2D receiver arrays on the Earth's surface, the role of density has been neglected. If density is assumed to be constant over space, equation (10) reduces to the scalar Helmholtz wave equation, the 2D version of which is usually used as a basis for WEI where ∇ is used as a 2D operator ($\nabla = \nabla^H = [\partial_x, \partial_y]^T$) and $\mathbf{x} = [x, y]^T$:

$$c_\omega(\mathbf{x})^2 \nabla^2 \vartheta(\mathbf{x}, t) = \partial_t^2 \vartheta(\mathbf{x}, t) \quad (24)$$

Here, ϑ denotes any type of wavefield quantity (e.g., one component of the wavefield displacement or particle velocity field, or the pressure field) which varies as a function of horizontal position \mathbf{x} and y and time t . This equation is a significant approximation to how seismic waves propagate in the Earth's subsurface: all

3D propagation of elastic body waves and of different types of surface wave, each associated with multi-component particle motions, are approximated by a single wave type propagating in 2D across the Earth's surface with a single independent component of particle motion. For example, in isotropic media Love waves are horizontally polarized and arrive most prominently on the transverse component, whereas the Rayleigh waves are polarized in a vertical plane and appear mainly on the vertical and radial components (Shearer, 2019). In the case of ambient noise, we deal with complex wavefields arriving from multiple sources which makes it impossible to distinguish radial contributions from transverse contributions; Love and Rayleigh waves therefore interfere in the horizontal particle velocity field yet are treated as one wave type in the 2D scalar wave equation. On land, 1C geophone recordings are usually employed as gradiometric measurements, because Rayleigh waves typically dominate the ambient seismic noise field and predominantly excite vertical displacements. A similar argument applies to Scholte waves which travel along the water-seabed interface. And since surface waves predominantly travel across the Earth's surface and have a dominant mode number, they are commonly approximated by superpositions of dispersive, single-mode plane waves that each satisfy the 2D scalar wave equation.

In order to improve the suitability of the Helmholtz approximation for surface waves, the wavefield is usually first filtered around a fixed frequency ω . WEI then proceeds by estimating all spatial and temporal derivatives in equation (24) given measurements of a passing wavefield made on a dense array. Thereafter the equation can be solved for the phase velocity c_ω . Nevertheless, the series of approximations above degrades the estimates of surface wave velocity.

In acoustic media however, the Helmholtz wave equation may be a reasonable model of wave propagation because the only approximation made in governing physics is that density is assumed to be locally constant across the array of receivers used to estimate spatial derivatives in ∇P . To account for a spatial variability in subsurface density, we consider the full acoustic wave equation in the time domain:

$$\nabla \cdot \left(\frac{1}{\rho(\mathbf{x})} \nabla P(\mathbf{x}, t) \right) = \frac{1}{\rho(\mathbf{x}) c_\omega(\mathbf{x})^2} \partial_t^2 P(\mathbf{x}, t) \quad (25)$$

The full acoustic wave equation represents the underlying physics that relates phase velocity c_ω and density ρ to dilatational wavefield observations where pressure P is used as wavefield quantity Φ . In acoustic media, equation (25) captures the full physics whereas it is only an approximation of wave propagation in elastic media. To perform WEI on the basis of the full acoustic wave equation in elastic media, we need to compute

the pressure wavefield P from equation (7) and substitute the resulting potential $\Phi = K_a \nabla \cdot \mathbf{u}$ into equation (10) where $\mathbf{u} = \mathbf{u}_H = [u_x, u_y]$ and $\nabla = \nabla^H = [\partial_x, \partial_y]$.

Using the foundation of the full acoustic wave equation we set up an inversion process to estimate both velocity and density from gradiometric measurements. We first parametrize the system in order to remove non-linearity in these forward relations. We simplify the form of equation (25) by introducing parameters $g(\mathbf{x})$ and $h(\mathbf{x})$ that vary as a function of horizontal position:

$$h(\mathbf{x}) = \frac{1}{K(\mathbf{x})} = \frac{1}{\rho(\mathbf{x})c_\omega(\mathbf{x})^2} \quad (26)$$

$$g(\mathbf{x}) = \frac{1}{\rho(\mathbf{x})} \quad (27)$$

The full acoustic wave equation then becomes

$$\nabla g(\mathbf{x}) \nabla P(\mathbf{x}, t) = h(\mathbf{x}) \partial_t^2 P(\mathbf{x}, t) \quad (28)$$

We rely on accurate knowledge of second order spatial gradients of pressure which can not be measured directly in the field. We calculate these gradients discretely using finite differences which are based around Taylor series expansions (Curtis and Robertsson, 2002). We discretize equation (28) on a horizontal, regularly spaced receiver grid at the surface (Fig. 2a) using classical central finite differences (FD) after (Geiger and Daley, 2003) to approximate the derivatives. Discretizing with the FD method does not require regular grids if we adopt a generalized FD scheme after (Liszka and Orkisz, 1980; Huiskamp, 1991; Gavete et al., 2003), however in our case receiver spacing Δx and Δy in x and y directions respectively are constant and equal, and indices i and j define receiver locations where i ranges from $[0, M]$ and j ranges from $[0, N]$. We formulate the discretized expression and rearrange the terms isolating the model parameter $g_{i,j}$ that contains information about subsurface density only:

$$\begin{aligned} \frac{1}{2\Delta x^2} \left[P_{[0,-]}^n g_{[i,j-1]} + P_{[-,0]}^n g_{[i-1,j]} \right. \\ \left. + P_{[\pm,\pm]}^n g_{[i,j]} + P_{[+,0]}^n g_{[i+1,j]} + P_{[0,+]}^n g_{[i,j+1]} \right] = h_{[i,j]} \left[\frac{P_{[i,j]}^{n+1} - 2P_{[i,j]}^n + P_{[i,j]}^{n-1}}{\Delta t^2} \right] \end{aligned} \quad (29)$$

where $P_{[0,-]}^n$ and $P_{[0,-]}^n$ are written similarly to

$$P_{[0,+]}^n = P_{[i,j+1]}^n - P_{[i,j]}^n \quad (30)$$

$$P_{[+,0]}^n = P_{[i+1,j]}^n - P_{[i,j]}^n \quad (31)$$

and

$$P_{[\pm,\pm]}^n = P_{[0,-]}^n + P_{[-,0]}^n + P_{[0,+]}^n + P_{[+,0]}^n \quad (32)$$

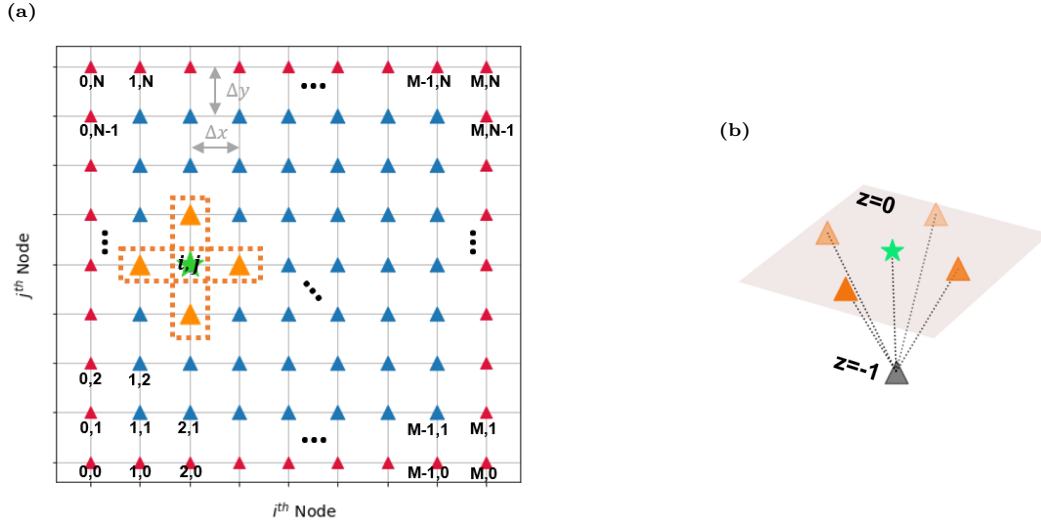


Figure 2: (a) Discretization of wavefield derivatives using a surface receiver grid, shown in plan view on the x-y plane. Receivers are marked by triangles (internal stations in blue, border stations in red). The grid has N rows in y-direction and M columns in x-direction. The pressure field P is recorded at each receiver position $[i,j]$. The classical second order finite difference stencil of receivers is represented by the cross-shape (orange), using which the second order derivative of the wavefield is estimated at the central point marked by the star symbol (green). (b) shows the corresponding buried receiver (grey) at 1m below the surface that is used for volumetric gradiometry across the finite difference cross-shaped stencil.

Equation (29) can be written in matrix form

$$\mathbf{A} \mathbf{g}_{\text{est}} = \mathbf{d} \quad (33)$$

where matrix \mathbf{A} has dimensions $[R \times R \times n_t]$ with R being the number of parameters over the receiver grid ($R = M \times N$) and n_t the number of data in the time series. \mathbf{A} contains purely observed data consisting of the pressure differences (equations 30 to 32) and is banded and square $[R \times R]$ for each time step n in the time series of the signal. Vector $\mathbf{g}^{\text{est}} = [g_{[0,0]}, g_{[1,0]}, \dots, g_{[M,N]}]^T$ is the parameter vector of dimension $[R \times 1]$ to be estimated, and \mathbf{d} is an observed data vector of dimension $[R \times n_t]$ that contains time derivatives

of the recorded pressure field $P_{i,j}$ multiplied by terms $h_{i,j}$ (right-hand side of eq. 29). Equally accurate calculations of derivatives at the corners and boundaries of the array are not possible since neighbouring receivers are not available in all directions so the full cross-shaped finite difference stencil (Fig. 2) can not be used and is depleted to a stencil formed by two or three adjacent stations only. We therefore introduce a weighting matrix \mathbf{W} that gives less weight to information from corner and boundary points of the receiver grid which are likely to provide less accurate constraints than the internal receivers. For corner and border receivers we chose a weighting factor very close to zero to minimize the impact on results while still maintaining the invertibility of matrix \mathbf{A} . Consequently, density estimates are evaluated only at internal receivers.

Since the density information is contained in both parameter vector \mathbf{g}^{est} and the vector \mathbf{d} through parameter vector $\mathbf{h} = [h_{[0,0]}, h_{[1,0]}, \dots, h_{[M,N]}]^T$, prior information is given in the form of an initial reference model for \mathbf{h} which we call \mathbf{h}^{init} :

$$\mathbf{h}^{\text{init}} = \frac{1}{\rho_{\text{init}} \mathbf{c}_{\omega, \text{init}}} \quad (34)$$

So as not to bias the inversion towards a heterogeneous solution, we chose a homogeneous reference for density ρ_{init} . The reference model $\mathbf{c}_{\omega, \text{init}}$ for phase velocity is obtained from an initial wave equation inversion using the standard scalar Helmholtz wave equation formulation (24) following the methods of De Ridder and Biondi (2015) and Cao et al. (2020). To stabilise the inverse problem we introduce generalized Tikhonov regularization:

$$[\mathbf{W}\mathbf{A} + \Theta_d \mathbf{I}] \mathbf{g}^{\text{est}} = [\mathbf{d} + \Theta_d \mathbf{g}^{\text{init}}] \quad (35)$$

Damping term Θ_d controls how strongly the solution is drawn towards the homogeneous reference model \mathbf{g}^{init} . We then find the least-squares solution for parameters \mathbf{g}^{est} that contain the density information

$$\mathbf{g}^{\text{est}} = [\sum_{n=1}^{n_t} (\hat{\mathbf{A}}_n^T \hat{\mathbf{A}}_n)^{-1} \hat{\mathbf{A}}_n^T] [\sum_{n=1}^{n_t} \hat{\mathbf{d}}_n] \quad (36)$$

where $\hat{\mathbf{A}} = [\mathbf{W}\mathbf{A}, \Theta_d \mathbf{I}]^T$ and $\hat{\mathbf{d}} = [\mathbf{d}, \Theta_d \mathbf{g}^{\text{init}}]^T$. After one iteration solving for \mathbf{g}^{est} , we obtain a first approximation to density that we note \mathbf{g}' . Substituting this density approximation into equation (25), we estimate phase velocity using gradiometric methods where we write the discrete finite difference form of equation (25) in terms of parameter \mathbf{g}' and estimate the phase velocity via linear regression similarly to (De Ridder and

450 Biondi, 2015):

$$\begin{aligned} \frac{1}{2\Delta x^2} \left[g'_{[0,-]} P_{[i,j-1]}^n + g'_{[-,0]} P_{[i-1,j]}^n - g'_{[\pm,\pm]} P_{[i,j]}^n \right. \\ \left. + g'_{[0,+]} P_{[i,j+1]}^n + g'_{[+,0]} P_{[i+1,j]}^n \right] c_{\omega,[i,j]}^2 = \left[\frac{P_{[i,j]}^{n+1} - 2P_{[i,j]}^n + P_{[i,j]}^{n-1}}{\Delta t^2} \right] \end{aligned} \quad (37)$$

451 where $g'_{[-,0]}$ and $g'_{[0,-]}$ are written similarly to

$$g'_{[+,0]} = \frac{g'_{[i+1,j]}}{g'_{[i,j]}} + 1 \quad (38)$$

$$g'_{[0,+]} = \frac{g'_{[i,j+1]}}{g'_{[i,j]}} + 1 \quad (39)$$

452 and

$$g'_{[\pm,\pm]} = g'_{[0,-]} + g'_{[-,0]} + g'_{[+,0]} + g'_{[0,+]}$$

453 In matrix form, equation (37) can be written

$$\mathbf{J}' \mathbf{m}' = \mathbf{d}' \quad (40)$$

454 where $\mathbf{m}' = [c_{\omega,[0,0]}^2, c_{\omega,[1,0]}^2, \dots, c_{\omega,[M,N]}^2]^T$ is the parameter vector of dimension $[R \times 1]$, \mathbf{d}' is an observed data
 455 vector of dimension $[R \times n_t]$ that contains time derivatives of the recorded pressure field and coefficient matrix
 456 \mathbf{J} of dimensions $[R \times R \times n_t]$ contains knowledge about the pressure wavefield gradients and density gradients
 457 from the full acoustic wave equation formulation. Information about density obtained from equation (36)
 458 and the updated phase velocity estimates obtained by solving equation (37) by linear regression or via
 459 least-squares WEI, provide an updated estimate of \mathbf{h} denoted \mathbf{h}' :

$$\mathbf{h}' = \frac{\mathbf{g}'}{\mathbf{m}'} \quad (41)$$

460 and \mathbf{g}^{init} is updated by \mathbf{g}' . We proceed to perform several iterations of solving equations (36) and (37) until
 461 we observe convergence towards a stable estimate of \mathbf{g}' . In the following we analyse this methodology for
 462 acoustic media, then test its performance in elastic media.

3.2 Volumetric arrays

To estimate density with volumetric gradiometry in an elastic medium, a 2-step procedure is implemented. First we discretise eq. (18) with finite differences on the volumetric array (Fig. 2b) and estimate body wave velocities with linear inversion techniques based on the free surface methodology described in Curtis and Robertsson (2002). We employ a standard non-regularized, least-squares minimization technique to estimate v_S' and v_P' . Second, we discretise left- and right-hand sides of eq. (23) with classical finite differences and substitute in the estimated body wave velocities v_S' and v_P' obtained from WEI:

$$\underbrace{\left[\partial_t^2 u_z + v_P'^2 \left[-\frac{2}{\Delta z} [\partial_z u_z]_{fd} + \nabla_H^2 u_z \right] - 2v_S'^2 \nabla_H^2 u_z \right]}_{\text{lhs}} \Big|_{[i,j,0]} = \frac{1}{\rho_{[i,j,0]}} \underbrace{\left[\frac{1}{\Delta z} \left(2 - \frac{4v_S'^2}{v_P'^2} \right) P \right]}_{\text{rhs}} \Big|_{[i,j,0]} \quad (42)$$

where,

$$\begin{aligned} \text{lhs}_{[i,j,0]} = & \frac{u_{z[i,j,0]}^{n+1} - 2u_{z[i,j,0]}^n + u_{z[i,j,0]}^{n-1}}{\Delta t^2} + v_{P[i,j,0]}'^2 \left[\frac{u_{z[i,j,-1]} - u_{z[i,j,0]}}{\Delta z} \right] \\ & + \left(v_{P[i,j,0]}'^2 - 2v_{S[i,j,0]}'^2 \right) \frac{u_{z[i,j-1,0]}^n + u_{z[i-1,j,0]}^n - 4u_{z[i,j,0]}^n + u_{z[i+1,j,0]}^n + u_{z[i,j+1,0]}^n}{\Delta x^2} \end{aligned} \quad (43)$$

$$\text{rhs}_{[i,j,0]} = \frac{1}{\rho_{[i,j,0]}} \left[\frac{1}{\Delta z} \left(2 - \frac{4v_{S[i,j,0]}'^2}{v_{P[i,j,0]}'^2} \right) P_{[i,j,0]} \right] \quad (44)$$

which enables density to be estimated via linear regression at each receiver position $[i,j,0]$ at the surface:

$$\text{lhs}_{[i,j,0]} = \frac{1}{\rho_{[i,j,0]}} \text{rhs}_{[i,j,0]} \quad (45)$$

4 Synthetic Tests

By using wavefield gradiometry we aim to image the shallow subsurface in as much detail as possible. With the following synthetic study we wish to examine the role of density in enhancing or obscuring our resolution of lateral heterogeneities.

We use the 3D wavefield modelling software Salvus (Afanasiev et al., 2019) to produce accurate synthetic acoustic and elastic wavefield recordings in 3D heterogeneous media. The wavefield is recorded at the surface over a 40×40 receiver grid in the middle of the domain. As a rule of thumb in gradiometry, the wavefield should be sampled at spatial points spaced a maximum of around 12% of the minimum wavelength apart,

in order to obtain an accuracy of 10% in first order spatial derivatives (Langston, 2007b). Analogous error calculations for second order derivatives suggest that for a same level of accuracy receivers must be spaced at a minimum of 24% of the minimum wavelength (Appendix A); in other words for the same receiver spacing, second order derivatives are less prone to large finite difference errors than first order derivatives. With a spacing of 2 m and a minimum medium velocity of 1550 m/s, this allows frequencies up to 180 Hz to be used with reasonable accuracy. All wavefields are recorded for a time interval of 3 s at a temporal sampling rate of 0.3 ms. A buried receiver is placed 1 m below every receiver on the surface array for volumetric gradiometry.

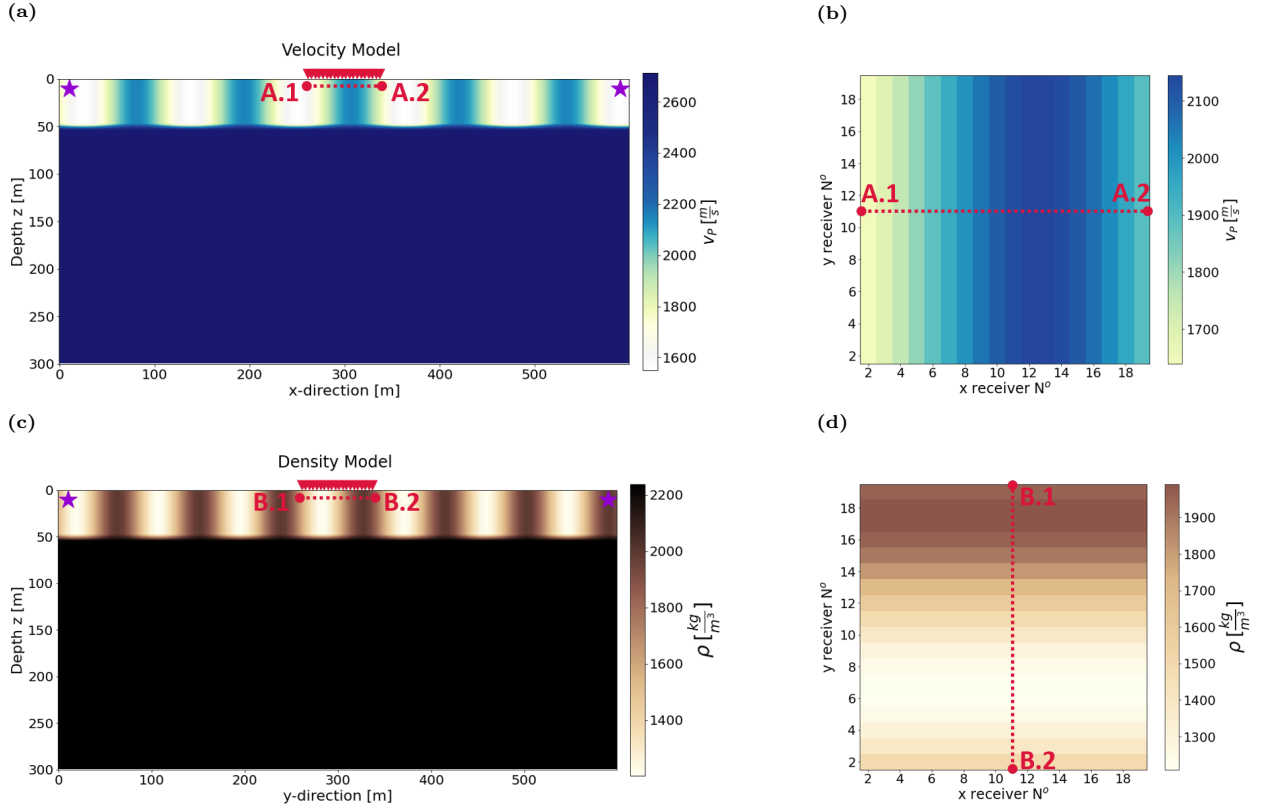


Figure 3: (a) Acoustic velocity model cross-section in xz-plane. Source locations relative to the receiver array are indicated by stars. Receiver groups marked by red triangles highlight the location of one line of 40 receivers at the surface and their corresponding buried receiver positioned at 1 m depth below. The total array spans an area of 78×78 m² spaced at 2 m intervals across the range [261, 339] m in both x and y directions. For gradiometry relying exclusively on the surface array, derivatives are calculated over a decimated receiver grid spaced at 4 m, whereas all surface receivers at 2 m intervals are used to perform volumetric gradiometry. All plan views showing model parameters are represented on the decimated grid at 4 m receiver spacing. (b) 2D xy-plan view map of the section of the true velocity model spanned by the internal receivers of the surface array. Depth boundary from layer 1 to layer 2 does not correspond to a step function change but a linear increase within the model cell that transitions between properties from the shallower layer to the deeper layer. (c) Density model depth cross-section in yz-plane. (d) 2D xy-plan view map of the section of the true density model spanned by the internal receivers of the surface array. For the pressure signals in Figure 4, a constant density model of 1600 kg/m³ is used instead for the top layer (Fig. B1). Elastic runs are performed with the same velocity and density structure and an additional shear-wave velocity field. Acoustic and elastic forward models have slightly different meshing criteria due to their respective minimum model velocities.

Relevant depth slices and plan view maps of the true acoustic P wave velocity and density model are shown in Figure 3. The velocity heterogeneity of the top layer follows a sine function in the x-direction at a wave-

length of approximately 113 m. The density structure has a wavelength of 88 m and is rotated by 90° respective to the velocity structure in order to clearly decouple influences of each parameter. The rotation of the orientation of density heterogeneities relative to those in velocity should reveal whether the estimated density structure contains artefacts caused by velocity heterogeneity and vice-versa. Layer 1 is 50 m thick and velocities span the range 1550 m/s to 2300 m/s, densities span 1200 kg/m^3 to 2000 kg/m^3 , while the deeper layer has a homogeneous velocity of 2700 m/s and density of 2240 kg/m^3 . The receiver array spans an area of $78 \times 78 \text{ m}^2$ and captures at least half a wavelength of the heterogeneity in both velocity and density structures (Figs 3b and 3d). Elastic models are constructed analogously to Fig. 3 with an additional S wave velocity model related to P wave velocity by a Poisson ratio of 0.25.

To test the performance of WEI for simulated ambient noise, five isotropic sources are placed on a circle around the receiver array at a radius of 290 m from the midpoint. They fire Ricker wavelet signatures with different central frequencies ranging from 4.5 Hz to 16 Hz at random time intervals but with the same amplitude to examine whether WEI is robust against waves of overlapping frequency. The sources fire close to the surface at 10 m depth to ensure that the dominant wave energy travels along the surface, allowing the assumption that the pressure gradient in z-direction is small compared to horizontal directions. The increasing velocity with depth in the model ensures that the waves are dispersive as in the true Earth's subsurface.

5 Density fingerprint

5.1 Free surface arrays

Sensitivity to relative density gradients in full acoustic wave equation

The full acoustic wave equation (25) can be written in the form of the Helmholtz wave equation and a source term containing relative density gradients $\nabla \rho(\mathbf{x})/\rho(\mathbf{x})$ acting on pressure gradients $\nabla P(\mathbf{x}, t)$:

$$\nabla^2 P(\mathbf{x}, t) - \frac{1}{c_\omega(\mathbf{x})^2} \partial_t^2 P(\mathbf{x}, t) = \frac{\nabla \rho(\mathbf{x})}{\rho(\mathbf{x})} \cdot \nabla P(\mathbf{x}, t) \quad (46)$$

Relative density gradients influence pressure gradients whenever a spatial density gradient $\nabla \rho(\mathbf{x})$, that is, a laterally heterogeneous density structure, exists. Otherwise the term on the right-hand side of equation (46)

becomes zero.

To illustrate the role that relative density gradients play in influencing wavefield gradients we conduct a synthetic experiment in which we compare Helmholtz and full acoustic spatial pressure gradients of a signal recorded at a single receiver station in the model shown in Figure 3 with variable density and velocity (Figs 4c and 4d) to one recorded in a model with the same velocity structure but where density is laterally homogeneous in the top layer at a fixed value of 1600 kg/m^3 (Appendix B, Fig. B1) corresponding to the mean value of the top layer in the variable density model (Figs 4a and 4b). The spatial pressure gradients are expressed as

$$\nabla^2 P(\mathbf{x}, t) \quad (47)$$

for the Helmholtz equation 24 and

$$\rho(\mathbf{x}) \nabla \cdot \left(\frac{1}{\rho(\mathbf{x})} \nabla P(\mathbf{x}, t) \right) \quad (48)$$

for the full acoustic equation (25). For simplicity of notation, we drop the indication of space and time dependencies of density ρ and pressure P hereafter. By comparing these spatial gradients in their discretized forms, we can establish a difference in discretization coefficients acting on pressure P , which subsequently influences the phase velocity estimates (Table 1). In the Helmholtz case, classical discretization coefficients for second order derivatives are used, whereas ratios of density from neighbouring receiver stations dominate the discretization coefficients in the full acoustic case (equations 37 to 40). If the pressure field passes through a homogeneous medium, the coefficients in the full acoustic case reduce to the Helmholtz coefficients since ratios of adjacent density values are equal to 1: the phase velocity estimates are thus identical in this case regardless of which equation is used for WEI. Whenever the densities between neighbouring receiver stations vary, the full acoustic coefficients contain density ratios not equal to 1 and an effect on the phase velocity estimate is expected depending on whether the Helmholtz or the full acoustic wave equation is used as a basis for WEI.

This behaviour of the spatial gradients becomes obvious in both acoustic (Figs 4a and 4c) and elastic (Figs 4b and 4d) media. In the homogeneous model case, Helmholtz and full acoustic spatial gradients are the same, resulting in no difference between Helmholtz and full acoustic spatial gradients (Figs 4a and 4b). In the model with variable density we observe a clear change in wave amplitude and a phase shift between

Table 1: If divided by receiver spacing Δx^2 , the presented values correspond to finite difference discretization coefficients on a regular grid (Fig. 2) for second order spatial pressure gradients in Helmholtz (24) and full acoustic (25) equations respectively. Helmholtz coefficients correspond to the classical central finite difference discretization values. Full acoustic coefficients are dependant on density ratios \mathbf{g}' of neighbouring receivers.

	[j-1]	[i-1]	[i,j]	[i+1]	[j+1]
Helmholtz:	1	1	-4	1	1
Full Acoustic:	$\frac{1}{2} \mathbf{g}'_{[0,-]}$	$\frac{1}{2} \mathbf{g}'_{[-,0]}$	$\frac{1}{2} \mathbf{g}'_{[\pm,\pm]}$	$\frac{1}{2} \mathbf{g}'_{[+,0]}$	$\frac{1}{2} \mathbf{g}'_{[0,+]}$

spatial gradients which is prominent between recording times 1 s and 1.7 s in the acoustic case. After 1.7 s changes in the shape of the waveforms of Helmholtz and full acoustic gradients are observed in the acoustic example (Figure 4c). Density gradients therefore create a clearly distinguishable fingerprint (Figs 4c and 4d), especially in acoustic media. The difference in Helmholtz and full acoustic spatial gradients is affected less strongly in elastic media even though underlying density gradient values are the same in both acoustic and elastic models. The fingerprint Γ is defined as the difference between normalised spatial gradients:

$$\Gamma = [\rho \nabla \cdot \left(\frac{1}{\rho} \nabla P \right)] - [\nabla^2 P] = \frac{\nabla \rho}{\rho} \cdot \nabla P \quad (49)$$

In the analysed synthetic model, density varies exclusively in the y-direction, where $\partial_x \rho = 0$ and Γ reduces to the form:

$$\Gamma = \frac{1}{\rho} \partial_y \rho \partial_y P \quad (50)$$

Neglecting information on density structure results in Helmholtz gradients that are not representative of the propagation medium. This causes the phase velocity to be either over- or underestimated by WEI when using the Helmholtz equation in a variable density medium.

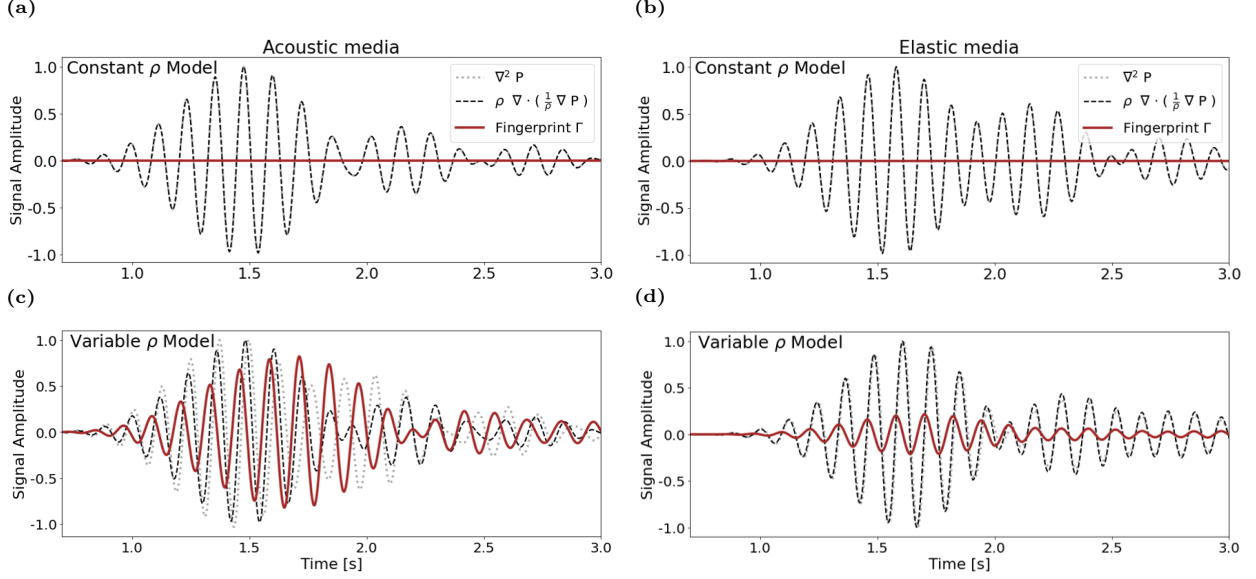


Figure 4: Effect of density gradients in 3D acoustic (a and c) and elastic media (b and d). Panel (a) and (b) show the discretized Helmholtz (dotted grey) and full acoustic (dashed black line) normalised spatial gradients at receiver [13,13] for a constant acoustic and elastic density model (Appendix B, Fig. B1) respectively. The difference between Helmholtz and full acoustic gradients (solid red line) shows that constant density has no influence on the measured wavefield. Panel (b) and (d) show the same information for a heterogeneous density model (Fig. 3c and 3d) in acoustic and elastic media respectively. The difference between Helmholtz and full acoustic gradients contains the signal generated by the density gradient in y-direction. The influence of the density gradient can clearly be distinguished (solid red line). In this example, the wavefield is filtered between 7 Hz to 9 Hz.

5.2 Volumetric arrays

Sensitivity to density in free surface fully elastic wave equation

The linear equation derived from the vertical component of the Lax-Wendroff corrected full elastic wave equation puts constraints on density directly. Equation (45) shows that density linearly relates the temporal and spatial derivatives of displacement to the pressure term. In Fig. 5 it becomes clear that the left- and right-hand sides of eq. (45) are related by a scaling factor. By fitting a regression line with the slope of the inverse of true density in the heterogeneous forward model, a coefficient of determination R^2 close to 1 is obtained suggesting that the scaling factor between left- and right-hand sides corresponds to the density of the medium. Fig. 5(b) shows that residuals are essentially zero between left-hand and right hand sides of eq. (45) if the true density is substituted. The density signal behaves analogously in homogeneous media.

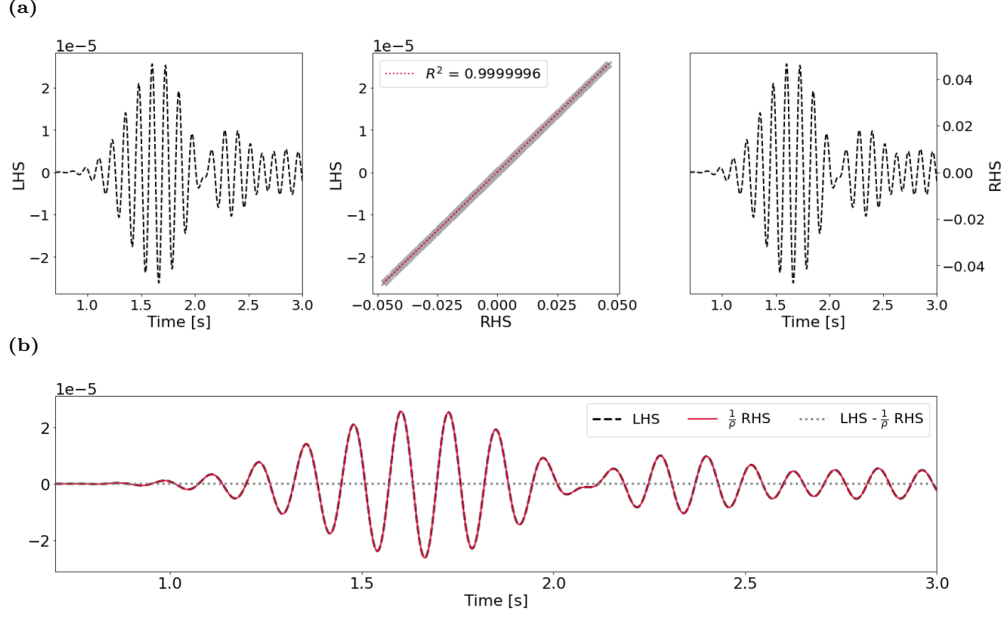


Figure 5: Role of density at the free surface of 3D elastic media (heterogenous forward model (Fig. 3)) shown at the example receiver at location [13,13]. The wavefield is filtered around a central frequency of 8 Hz with a bandpass of 2 Hz. Panel (a) shows the waveform of the discretised left-hand side (left column) and right-hand side (right column) of eq. (45) when true velocity model parameters are used. The middle column in (a) shows a scatter plot of left- and right- hand data with a regression line of a slope corresponding to the inverse of true density at receiver [13,13]. R^2 is the coefficient of determination defining the goodness of fit of the regression line and the data. Panel (b) shows the residuals (LHS - $1/\rho$ RHS) between left- and right-hand side of equation (45) if the true model density is used.

6 Inversion Results

We now present results from the iterative inversion process for density and phase velocity using simulated ambient noise. In section 6.1.1 we investigate the performance of density estimation in acoustic media at a central frequency of 8 Hz where the wavefield data is filtered with a narrow bandpass in the range 7 Hz to 9 Hz. We then show how the obtained density information affects the accuracy of phase velocity estimates based on WEI of the full acoustic wave equation, and how random noise impacts the robustness of these estimates. We then investigate the quality of density inversion over a broader frequency range from 4 Hz to 14 Hz and the impact that full WEI has on estimates of phase velocity dispersion curves. In section (6.1.2) we discuss the estimated density results in elastic media for a wavefield filtered around 8 Hz obtained with the same iterative inversion workflow. Misfit functions are presented to illustrate trade-offs between density and phase velocity in both acoustic and elastic media (Section 6.1.3). We then show the density results in elastic media, obtained by gradiometric linear regression from the full elastic wave equation at the free surface (Section 6.2).

6.1 Free surface arrays

6.1.1 Acoustic Data

Density Estimation

Figure 6(a) shows the density inversion results as a mean over all cross sections in x (Fig. 6a, left) and y direction (Fig. 6a, right). Corresponding lateral relative y- and x-gradients in density are depicted in Figure 6(b) in the left and right column respectively. Without damping, there is no constraint on the absolute value of the density. Hence, the inversion process is quite sensitive to different initial damping parameters Θ_d . As a rule of thumb, setting the initial damping parameter at 10% of the mean amplitude of all recorded pressure signals stabilized our inversions. The mean value over the true density model is fed to the inversion as the initial homogeneous guess ϱ_{init} .

We clearly see the effect of the damping term in the first iteration where the inverted density estimate is skewed towards the initial guess. After the initial iteration we decrease the damping parameter by a factor of 10 and keep it constant for a total of 100 iterations. Lowering the damping parameter gives less weight to the prior information. Tests showed that the inversion process is only sensitive to the initial damping parameter: decreasing the damping parameter further after the initial stabilization phase did not have an effect on the final result, but it allowed the inversion to converge faster towards a minimum misfit solution. After only 10 iterations of alternately updating velocity and density, the density estimates approximate the true solution fairly well and remain stable over subsequent iteration steps until the end of the inversion process is reached. The initial spiky character observed in x-direction might arise since we did not impose any smoothness constraints on the inversion. The logarithm of the data misfit vector δ_d of dimension $[R \times 1]$

$$\delta_d = \frac{\sum_{n=1}^{n_t} (\mathbf{J}'_n \mathbf{m}' - \mathbf{d}_n)^2}{n_t} \quad (51)$$

for the predicted model at each iteration is shown in Figure 6(c) and is used to determine whether the iteration delivers satisfactory results. At the initial iteration the logarithm of the full acoustic misfit of -7.0 is comparable to the Helmholtz misfit level at a value of -6.1. From there, the data misfit continually decreases with progressing iteration steps. In the first 10 iterations, the logarithmic misfit decreases rapidly from -7.0 to -13.2 at iteration 10. This steep drop correlates well with the improvement on the relative parameter error on the relative density gradient in y-direction. The relative error of parameter p at each location i,j is defined as the difference between the absolute values of true and estimated values $|p|^{\text{true}}$ and

608 $|p|^{\text{estimate}}$ divided by the true values

$$|\text{Error}|_{i,j} = 100 \left| \frac{|p|_{i,j}^{\text{true}} - |p|_{i,j}^{\text{estimate}}}{|p|_{i,j}^{\text{true}}} \right| \quad (52)$$

609 where, in this instance, parameter p stands for the relative x- or y-density gradients $\partial_x \rho / \rho$ and $\partial_y \rho / \rho$ re-
 610 spectively but can stand for any other estimated quantity. After 12 iterations the logarithm of the misfit
 611 remains almost constant around a value of -13.5 and only improves marginally to -13.9 until the inversion is
 612 stopped at iteration 100. The density gradient result with minimum parameter error to the true model in
 613 x-direction is achieved at iteration step 21.

614

615 The slight increase in parameter error on density thereafter is likely to originate from the velocity updates
 616 dominating the misfit evolution. Velocity has a much stronger effect than the density since it appears squared
 617 in the full acoustic wave equation. We showed in Figure 4 that in a medium with homogeneous density the
 618 spatial gradient expressions from the Helmholtz and the full acoustic equation are identical and so phase
 619 velocity estimates remain unaffected by homogeneous densities across the array. Since density is constant
 620 in the x-direction, the true phase velocity is only dependent on density structure in the y-direction. Given
 621 the poor constraints on density in the x-direction the mean estimate on the density gradient in x-direction
 622 deviates, if only slightly ($\pm 0.15\%$), from the true value of zero (Fig. 6b). This introduces artefacts in
 623 the phase velocity estimates which in turn influence density estimates negatively throughout the iterative
 624 process. Nevertheless, in our experiments the data misfit minimum does tend to indicate when parameter
 625 estimates are reasonably accurate. Cross-talk between density and velocity appears to be weak as density
 626 structure of the true model could be reconstructed successfully with reasonable accuracy without major
 627 artefacts (Fig. 6).

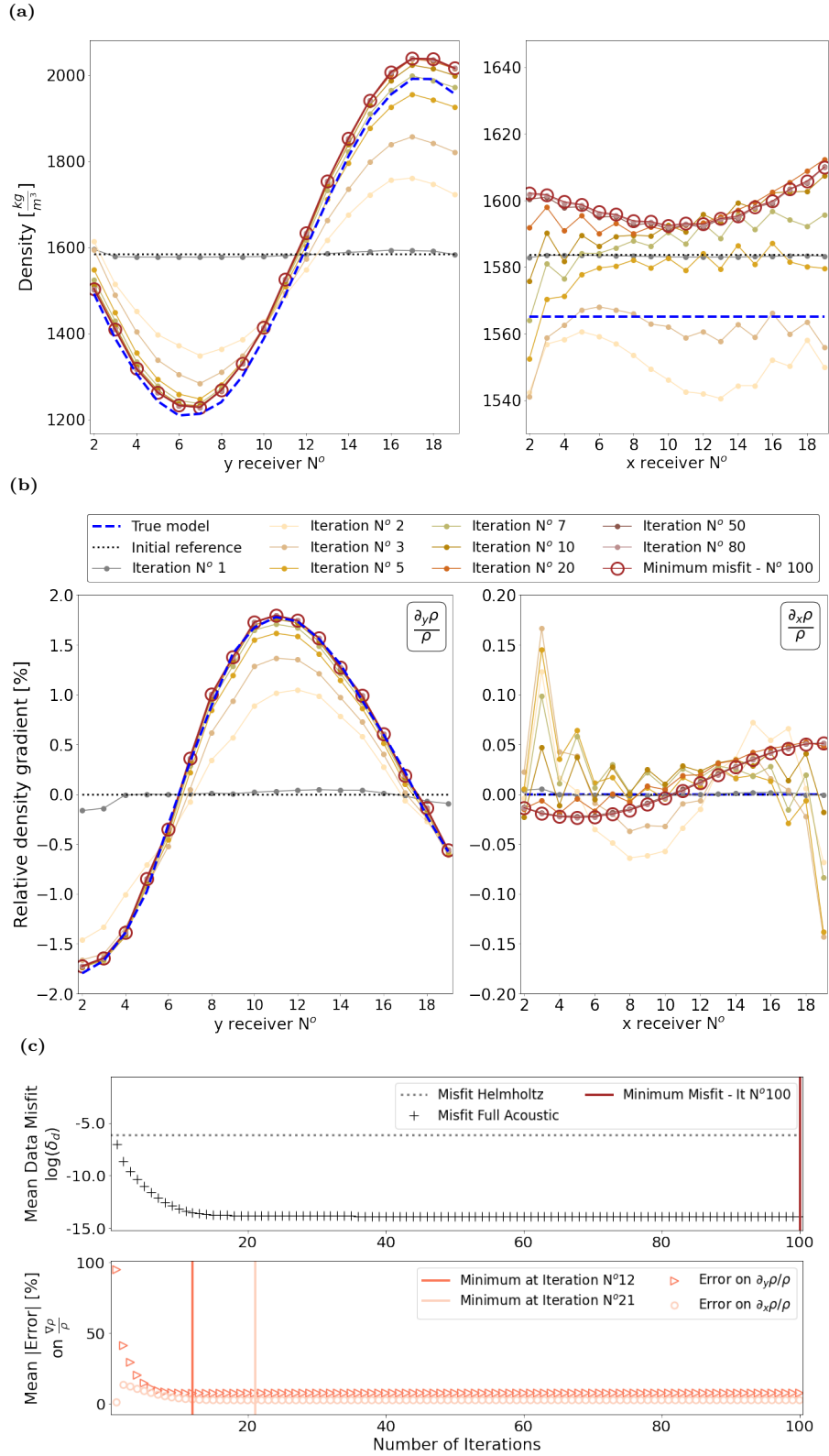


Figure 6: Inversion result for a wavefield filtered to include frequencies in the range of 7 Hz to 9 Hz. Only the results for the internal receivers 2 to 19 are displayed, as boundary stations need to be disregarded for finite difference estimates. (a) Mean value of inverted density results over all cross-sections in x-plane (left) and y-plane (right) showing the evolution of inverted density results at selected points during 100 iterations. True model is depicted as dashed dark blue line and initial model as dotted black line. The minimum misfit result at iteration 100 is highlighted by red circles. (b) Relative density gradients $\nabla \rho / \rho$ of (a) in y- and x-direction respectively. (c) Logarithm of the mean data misfit evolution over all internal receivers (upper row) and mean parameter error over all internal receivers on x- and y- relative density gradients (lower row) for the full acoustic wave equation (black crosses) over 100 iterations. Their respective minimum value positions are marked by vertical lines in red for minimum misfit at iteration 100, dark orange and light orange at iteration 12 and 21 for minimum parameter error on relative density y- and x-gradients. As a reference, the misfit achieved with linear regression based on the Helmholtz equation is shown by the dotted grey line. The minimum mean parameter error is evaluated only after the initial iteration.

As discussed in section 5, the inversion is predominantly sensitive to the relative changes in density $\nabla\rho/\rho$ where $\nabla\rho$ corresponds to the gradient of density at a central point $\rho = \rho_{i,j}$ over the finite difference stencil (cf. Fig. 2), and is less so to the absolute values $\nabla\rho$ (Fig. 7). Figure 7 shows that the minimum misfit estimate of the local density gradient in the y-direction is typically within $\pm 10\%$ of the true value for relative density changes larger than 0.5% over the width of the spatial finite difference stencil. The accuracy of estimates decreases for very weak relative changes below 0.5%. Estimates on absolute values may be biased depending on which initial density guess is fed to the first iteration of the inversion. Results in Figure 6(a) could successfully reconstruct absolute density values due to an appropriate choice of starting model ρ_{init} . If the initial guess of bulk density varies more strongly from the true values, the absolute estimates are under- or over-estimated according to the input starting model (Fig. 7a, left) because the inversion fits the relative changes in density ratios (Fig. 7a, right) as becomes obvious from equation (46). By reconstructing relative density changes, the results are unbiased by the choice of initial density model ρ_{init} (Fig. 7a, right). The results of relative density gradients for each local receiver position over the entire grid are shown in Figure 8 as 2D plan view maps.

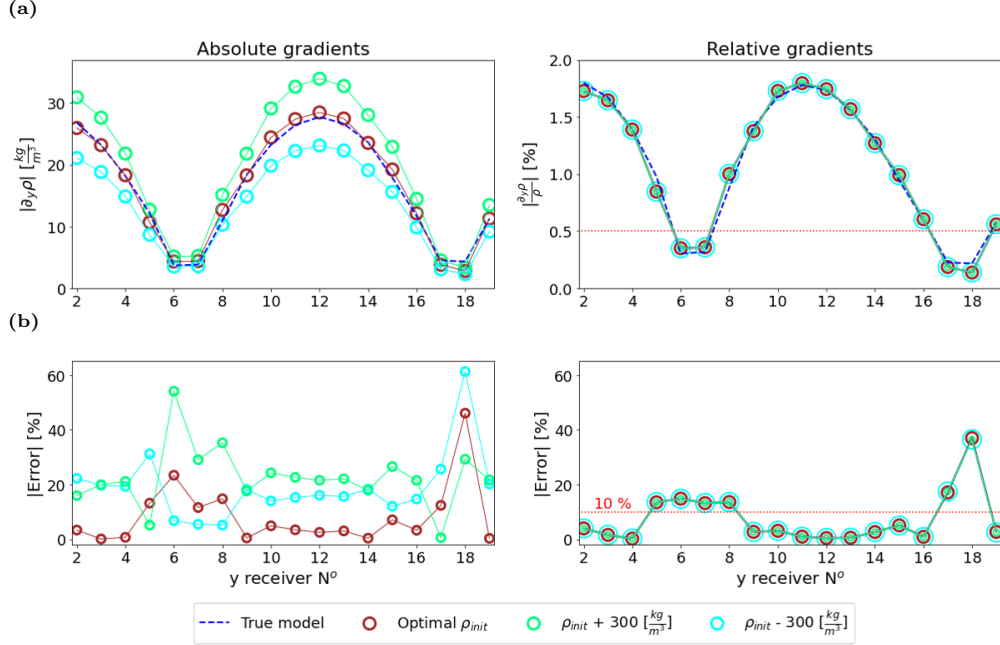


Figure 7: Impact of initial density guess ρ_{init} on inversion results of (a) absolute density y-gradients $\partial_y \rho$ (left) and relative density y-gradients $\partial_y \rho / \rho$ (right). Their respective errors are depicted in (b). Results from an optimal ρ_{init} starting model (red circles) correspond to the estimates in Figure 6(a) where ρ_{init} is the mean bulk density of the true model (dashed dark blue line). Results for a less well informed initial guess with higher mean bulk density (green circles) and lower mean bulk density (light blue circles) are shown for comparison.

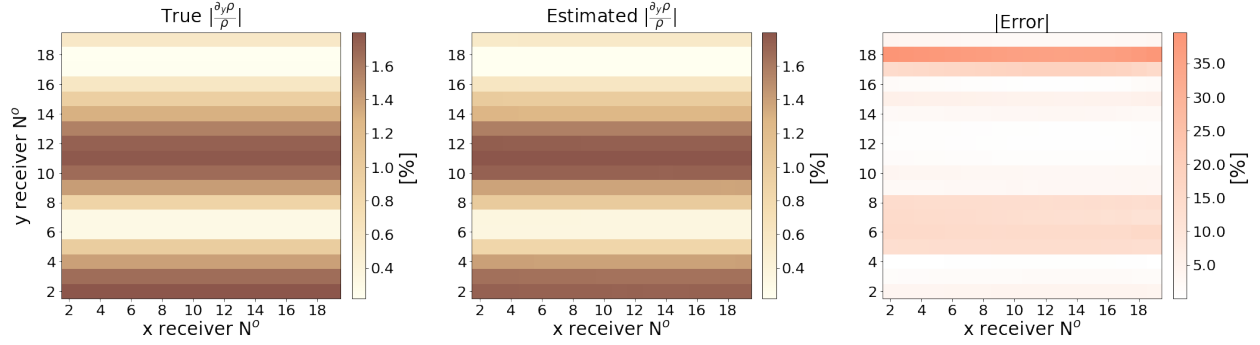


Figure 8: Plan view of (left) true model and (middle) inversion results for absolute values of relative density gradients in y-direction $\partial_y \rho / \rho$ at iteration 100. The corresponding parameter error (Eq. 52) is shown in the right panel.

Effect of density gradient on phase velocity estimates

We now show the extent to which the estimated density structure influences the accuracy of the phase velocity maps. Figure 9(a) shows the phase velocity map estimated using the same data as above, but with the Helmholtz wave equation, so without taking density into account in the formulation of wave propagation. Figure 9(b) shows phase velocity estimates based on the full acoustic wave equation at iteration 100 where the data misfit is minimal.

By visually comparing these maps to the true velocity structure (Fig. 3b) it is obvious that the Helmholtz approach fails to reproduce the relative structure of the subsurface velocity pattern. By contrast, the results obtained by WEI of the full acoustic wave equation yield an improved estimate of the velocity structure that is much closer to the true model in terms of relative structural features. This observation is reflected in the much lower misfit values obtained for the full acoustic model compared to the Helmholtz model (Fig. 9c). It is notable how the misfit evolution over the y-axis is dominated by the slope of the density heterogeneity in the true structure (red dashed line). The Helmholtz misfit values approach the full acoustic misfit values at a density gradient close to zero (see green highlight at y-receiver 6 in Fig. 9(c)), whereas, for steep changes in density at y-receiver 13 in the model, the Helmholtz equation performs relatively poorly.

Figure 10 illustrates the effect of density gradients on phase velocity estimates at two specific receiver stations in the array. Phase velocity squared is given by the slope of the linear relationship between spatial and temporal gradients (Equation (24) for Helmholtz and (25) for full acoustic equation). Figure 10(a) shows that the full acoustic spatial gradients reveal a clearer linear relationship than the Helmholtz model as indicated by a coefficient of determination R^2 closer to 1. The difference in best fit slope estimates shows that phase velocity is considerably underestimated for the Helmholtz model at receiver [13,13] due to the fact

that the relative density structure is neglected in the computation of the spatial gradients. This disparity in the accuracy of phase velocity estimates becomes evident also in the comparison of left-hand and right-hand side signals of the full acoustic and Helmholtz equation (Fig. 10b) and their respective residuals (Fig. 10c). They illustrate that the full acoustic expression matches the pure data vector well, whereas the Helmholtz expression exhibits larger residuals than the full acoustic case for both receiver stations. Incorporating density in the spatial gradient terms of WEI is thus shown to be important in order to estimate phase velocities accurately.

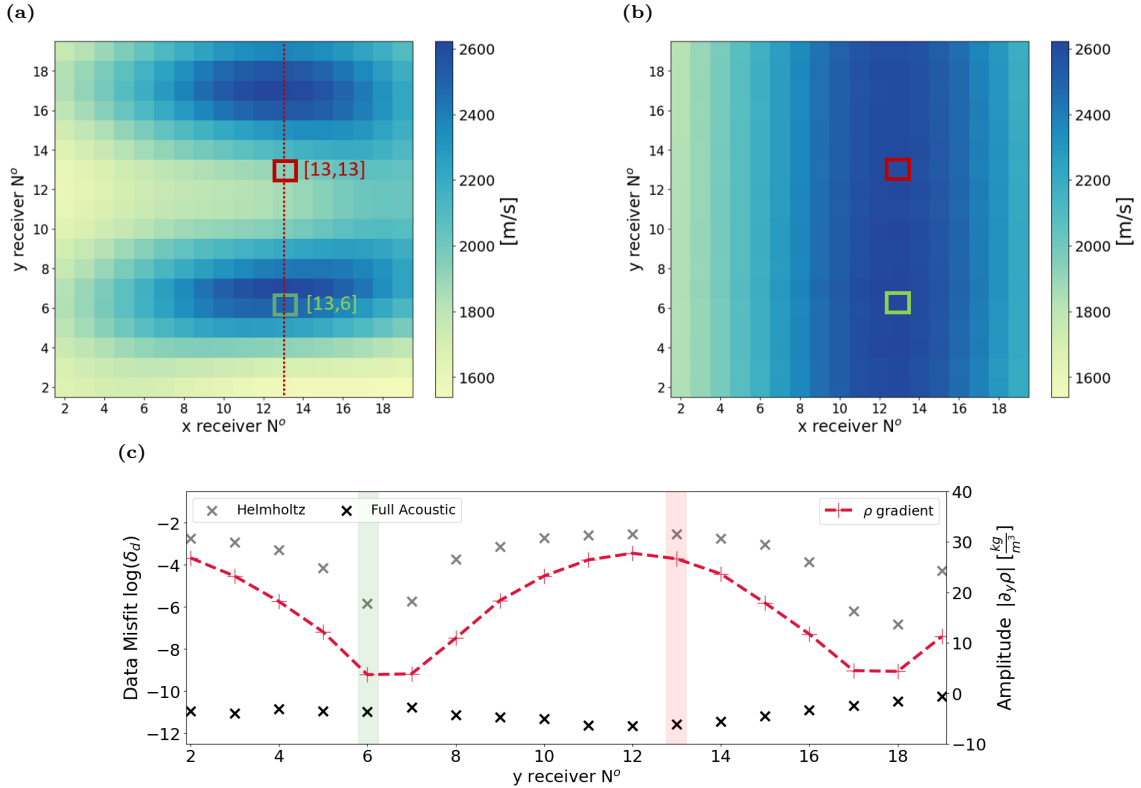


Figure 9: Phase velocity map estimated using (a) linear regression based on Helmholtz wave equation and (b) full acoustic wave equation inversion. Red and green squares mark receiver stations of interest [13,13] and [13,6]. (c) Data misfit post inversion averaged over all x-cross sections (red dotted line in (a) given at example of fixed receiver position $x=13$) for both phase velocity maps (a) and (b). Black and grey crosses show the logarithm of misfit δ_d in equation (51) for the Helmholtz equation (grey) and the full acoustic wave equation (black). The red dashed curve shows the absolute value of the y-gradient of the true density heterogeneity $\Delta\rho$. Green and red highlighting at receiver station 6 and 13 represent the respective positions in the 2D plan view map.

If we compare the misfit residuals for receiver [13,13] (Fig. 10c, left) and [13,6] (Fig. 10c, right), we can see that the full acoustic residuals are of the same order of magnitude at both stations whereas the Helmholtz residuals are two orders of magnitude larger for receiver [13,13]. Receiver [13,13] is located in an area where density is highly variable between the surrounding stations (26 kg/m^3 from Fig. 9c) which explains why the Helmholtz wave equation is subject to much larger residuals than the full acoustic equation. Receiver [13,6] is in an area with only weak variations in density among neighbouring receivers (4 kg/m^3 from Fig. 9c), so

the left-hand sides of both Helmholtz and full acoustic equations agree well with the observed data vector. The accuracy of velocity estimates thus depends on the true density gradient across surrounding receivers when using the Helmholtz equation for WEI.

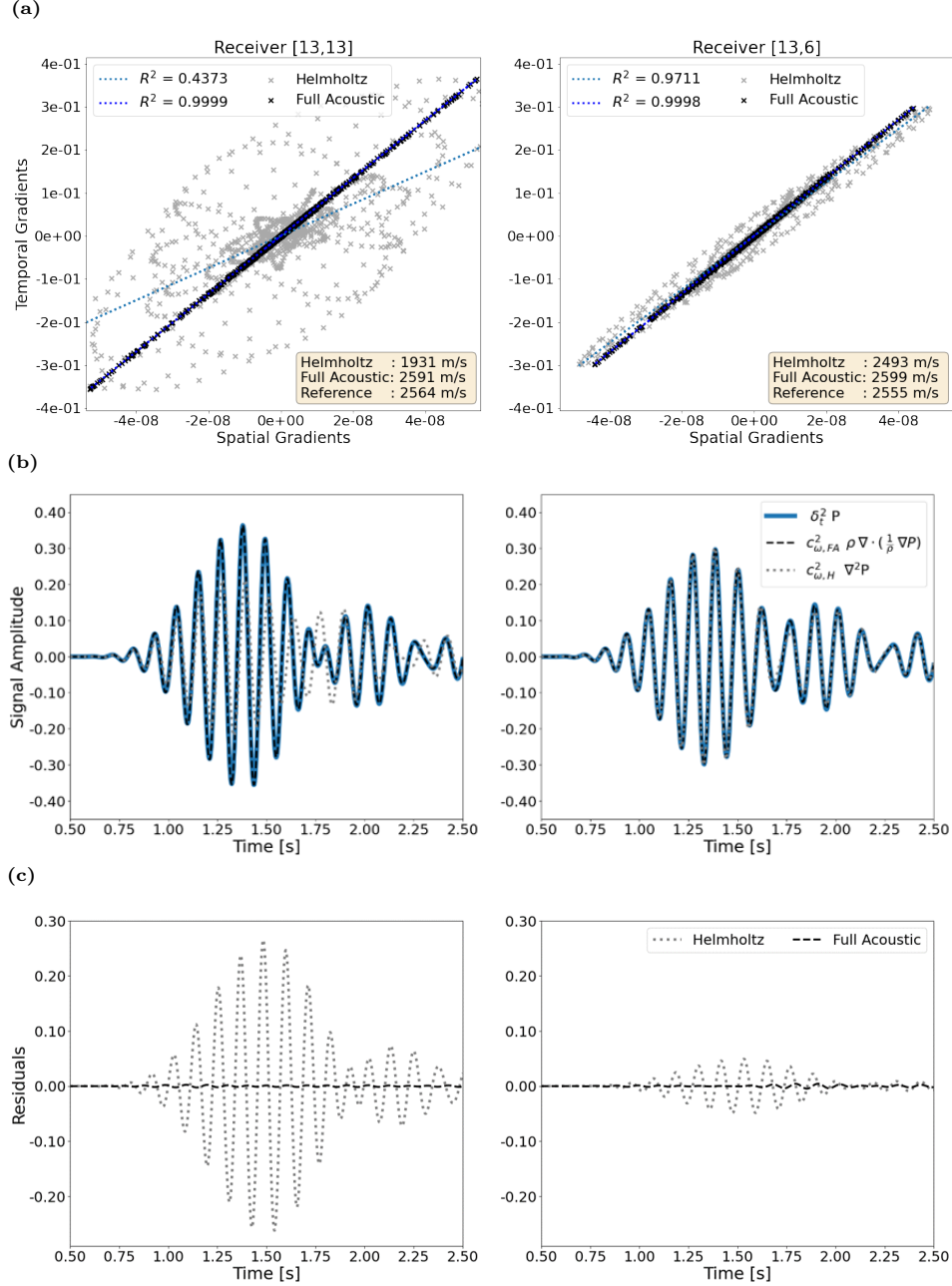


Figure 10: (a) Linear relationship between temporal gradients $\delta_t^2 P$ and $\rho \nabla \cdot (\frac{1}{\rho} \nabla P)$ from (48) for the full acoustic wave equation and $\nabla^2 P$ from (47) for the Helmholtz wave equation at the two receiver locations shown in Figure 9(a). The coefficient of determination R^2 denotes the goodness of fit of the data by the linear regression model, and phase velocity estimates using each equation are shown along with the reference velocity obtained for a homogeneous density forward model. (b) Discrete time series of the observed data vector ($\mathbf{d} = \delta_t^2 P$, solid blue) and the left-hand sides of both Helmholtz ($c_{\omega,H}^2 \nabla^2 P$, black dotted) and full acoustic ($c_{\omega,FA}^2 \rho \nabla \cdot (\frac{1}{\rho} \nabla P)$, grey dashed) wave equations respectively, when using the estimated parameter values for phase velocity and density. (c) Respective residuals (difference between right-hand and left-hand side) of both Helmholtz and full acoustic wave equations.

Changing data frequencies

The effect of the density gradient on phase velocity is persistent over a wider frequency range than was analysed above (Fig. 11a). In Figs 11(a) and 11(b), the dashed blue lines depict the true constant P-wave velocity in y- and x-direction respectively for the shallow layer 1 and the deeper layer 2 of the synthetic model (Fig. 3). Due to wave dispersion, the estimated phase velocities should lie in between those two expected absolute thresholds depending on the analysed frequency. The Helmholtz estimates for phase velocity (Fig. 11a) are consistently underestimated for receivers where density gradients are high (see Fig. 12 as reference), due to the use in WEI of discretization coefficients that neglect the influence of density (Table 1), whereas they approximate full acoustic (Fig. 11b) phase velocity estimates at low density gradient values. However, the influence of the density gradients on the Helmholtz phase velocity estimates seems to become smaller with increasing frequency.

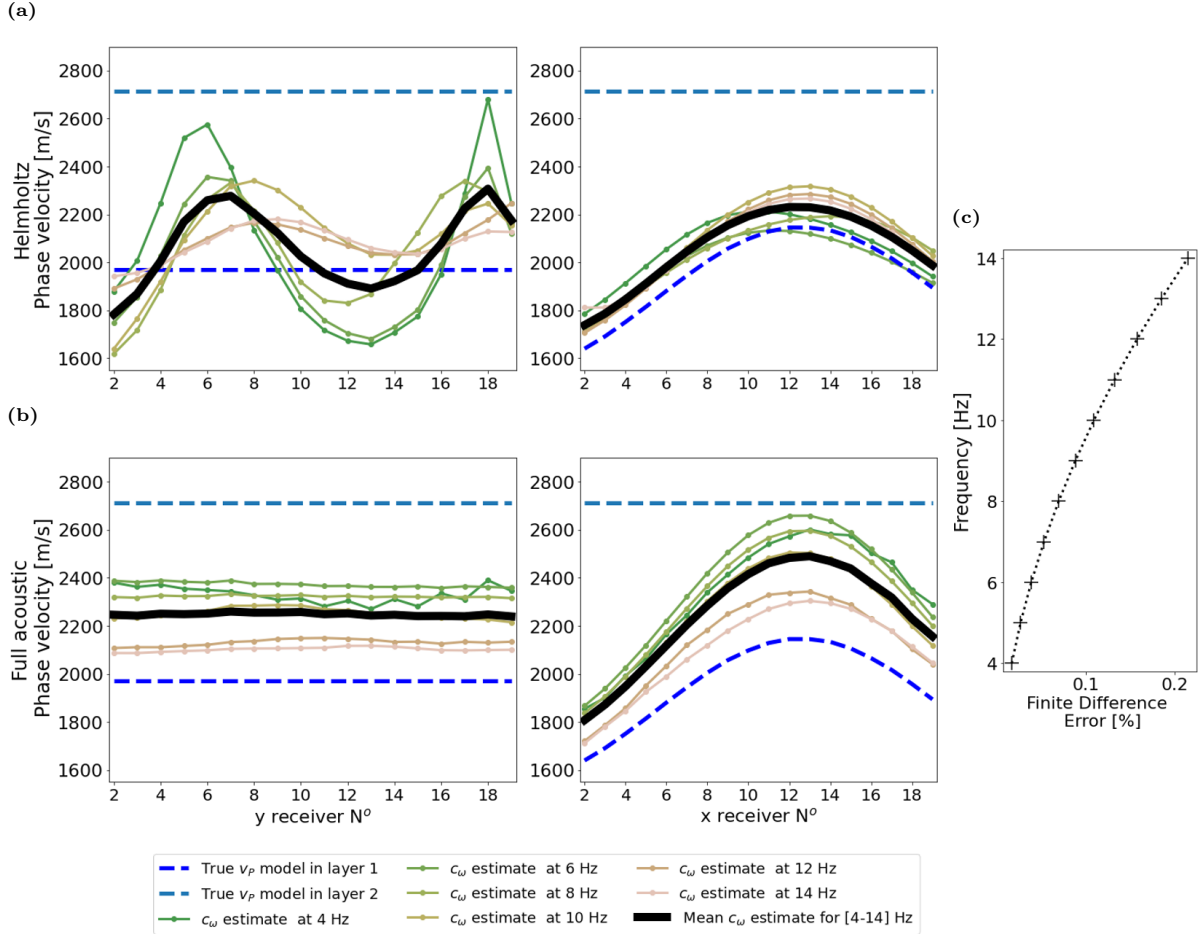


Figure 11: Results for the estimated phase velocities for 2 Hz wide bandpasses around central frequencies 4 Hz, 6 Hz, 8 Hz, 10 Hz, 12 Hz and 14 Hz from Helmholtz linear regression (a) and full acoustic WEI (b). For the estimation of full acoustic phase velocities, density information as shown in Figure 12 is used. The mean value over all the frequency results is shown for both full acoustic and Helmholtz velocities in a black solid line. (c) shows the error evolution over frequency for the 2nd order accurate approximation of the spatial gradients with a spacing of 4 m used in this example (see Appendix A).

Accuracy of density gradient estimates seems to decrease with increasing frequency (Figure 12): at a frequency of 4 Hz, the true gradient model in layer 1 is well approximated, whereas the result at frequency 14 Hz shows a clear discrepancy between true and estimated density gradients. A trend between errors on density gradients and strength of the density fingerprint (Fig. 12, right) becomes noticeable: parameter errors on estimated density gradients via WEI increase with decreasing strength of the density signal. This suggests that higher frequencies are less sensitive to density.

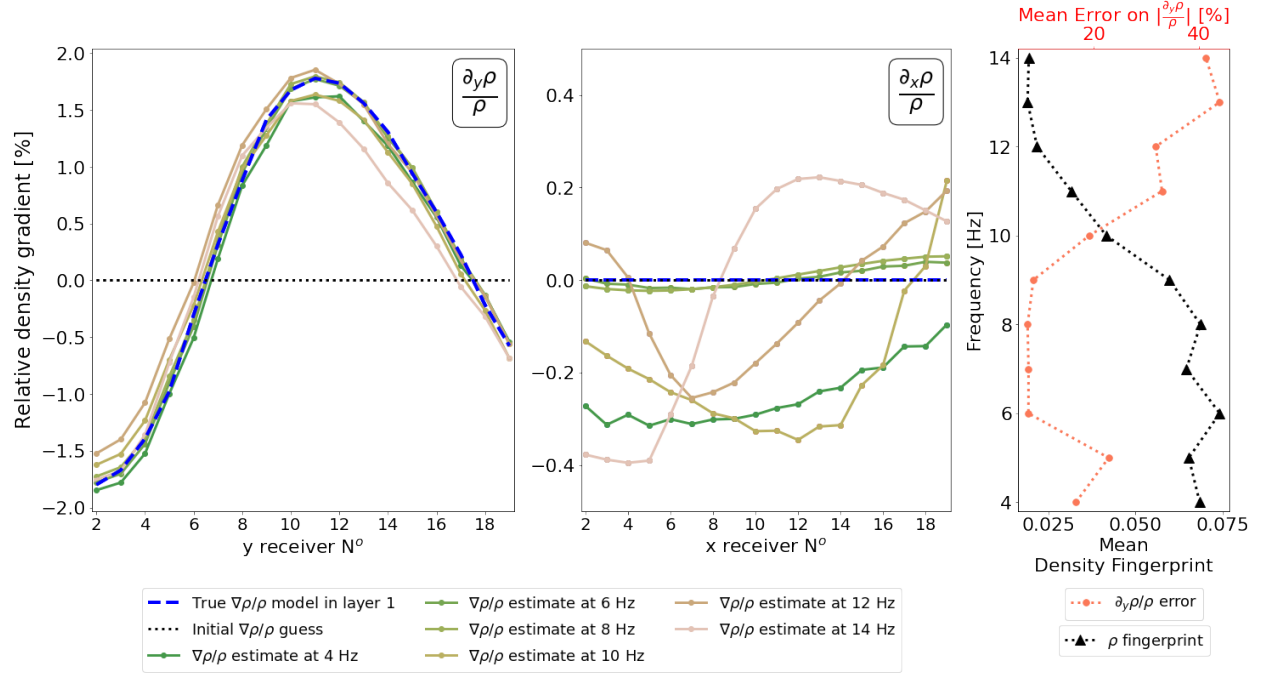


Figure 12: Results for density inversion at the lowest misfit iteration for 2 Hz wide bandpasses around central frequencies 4 Hz, 6 Hz, 8 Hz, 10 Hz, 12 Hz and 14 Hz. Estimated density is shown as a mean over all x (left panel) and y (middle panel) cross-sections respectively. The right panel shows the mean error (Eq. 52) on relative y-gradients of density averaged over the whole array per analysed frequency. The mean density fingerprint (Eq. 49) is calculated for each frequency as $1/n_t \sum_{n=1}^{n_t} |\Gamma_n|$ and then averaged over the array.

Figure 13(d) shows how phase velocity perturbation increases with decreasing frequency and is roughly correlated with the signal strength of density. Full acoustic WEI can account for these density induced effects in phase velocity over a broad range of central filter frequencies, producing more accurate dispersion curves (Figs 13a to 13c). The full acoustic estimates display higher coefficients of determination (Fig. 13b) and lower misfits (Fig. 13c) than the Helmholtz results over all frequencies. As a reference we estimate a dispersion curve for the velocity model in Figure 3 with a constant density of 1600 kg/m^3 in layer 1 (Appendix B, Fig. B1) and compare it to dispersion curves obtained with full acoustic and Helmholtz WEI (Fig. 13a) for the variable density model (Fig. 3). The dispersion curve calculated on the basis of full acoustic WEI is able to reproduce the general trend of the reference dispersion curve. We do not expect a perfect match as the imposed density structure in the laterally heterogeneous case does influence the paths taken by wave

energy. The Helmholtz dispersion curve does not reproduce the key feature of a classical dispersion curve where phase velocity increases with decreasing frequency. This shows that it is detrimental for depth model reconstruction to assume a constant density over space in a medium with laterally heterogeneous density, especially at lower frequencies.

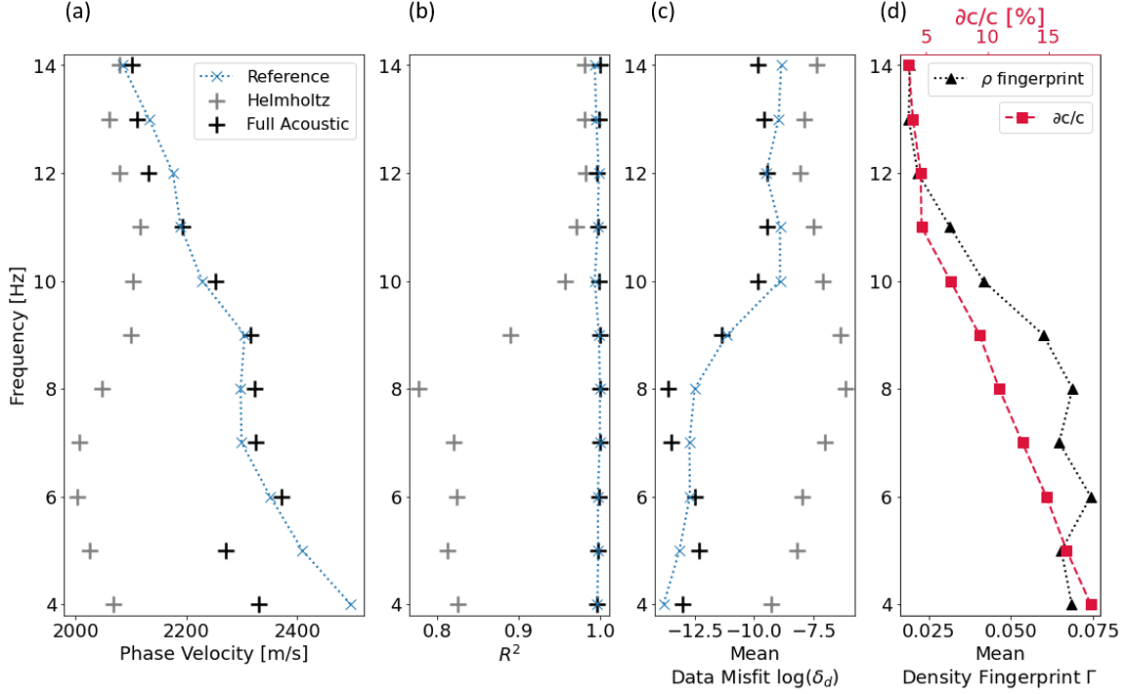


Figure 13: Mean phase velocity dispersion curve (a) over the whole array obtained via Full Acoustic WEI (black crosses) and Helmholtz WEI (grey crosses) respectively. Phase velocity results are obtained for a reference model (blue dotted line with cross marker) produced by the same setup as described in Figure 3 but with constant density in layer 1 (Appendix B, Fig. B1). Corresponding coefficients of determination (b) and misfits (c) are shown to evaluate the data fit. (d) The perturbation of phase velocity $\frac{\partial c}{c}$ (red dashed line with square markers) is defined by the difference between phase velocity in the heterogeneous (grey crosses) and homogeneous baseline model (blue crosses) obtained via linear regression on the basis of the Helmholtz wave equation. The mean fingerprint Γ of the density signal is defined as in Fig. 12 and shown by black triangles.

Random noise

Given that in real use case scenarios WEI depends on field recordings, it is important to consider the robustness of density estimation to errors in the recorded signal. The density signal is relatively weak compared to that of phase velocity, hence it may be obscured by instrumentation noise in the field. We add random noise, expressed as a percentage of the mean trace amplitude over the whole grid, to the simulated observed signals in order to determine a threshold of noise beneath which the method still delivers meaningful results. For each receiver, the added noise follows an uncorrelated normal distribution with a spread of 0.1 to 5% of the mean trace amplitude.

Correlation factors for density decrease with increasing noise levels. At noise levels 0.1 to 1% of the mean

722 trace amplitude, the pressure with added noise remains relatively similar to the true pressure (Fig. 14a). The
 723 density distributions are thus centred around the optimal correlation line where true and estimated density
 724 match perfectly (Fig. 14b). At a random noise level of 5% the density distribution does not approximate
 725 the optimal correlation line well which suggests that the relative density structure cannot be estimated
 726 accurately. The correlation of phase velocity is dominated by the quality of the density information and
 727 vice-versa: correlation coefficient values follow the same deteriorating trend when the noise level becomes
 728 higher (Fig. 14c). The estimates for both phase velocity and density remain stable up to a noise level of 1%,
 729 but even at a noise level of 5% the main structural trends are still recognised.

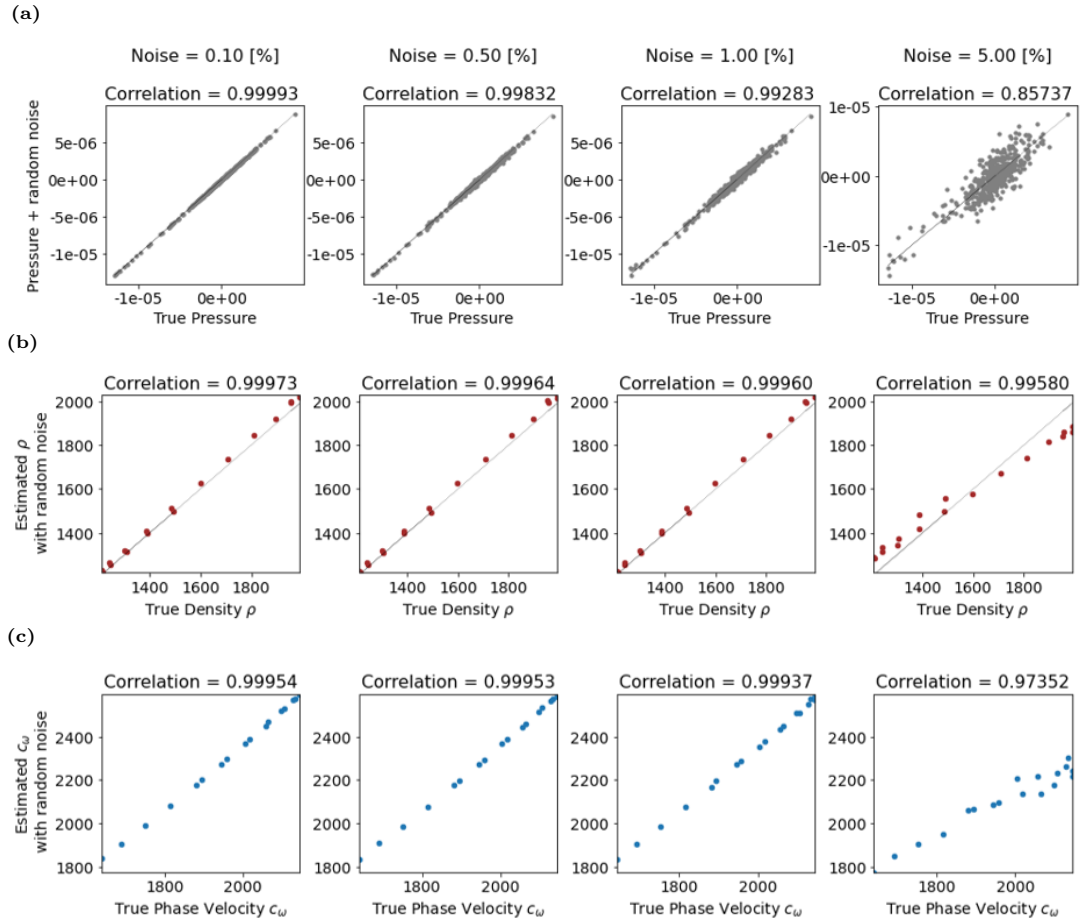


Figure 14: (a) Correlation plots between true pressure signal and pressure signal with added random simulated instrumental noise at 0.1 %, 0.5 %, 1 % and 5 % of the mean amplitude of the modelled pressure signal over the whole grid. Wavefield arrivals at $t > 2s$ are used to visualise the effect of the added random noise on lower amplitude signals. Correlation plots of model material parameters at the various noise levels; between true and estimated (b) density and (c) phase velocity. True phase velocity is taken as $0.9v_s$ of the surface layer, hence the frequency dependence is not taken into account as it is difficult to determine the expected phase velocity in a laterally heterogeneous medium.

6.1.2 Elastic Data

The iterative full acoustic inversion procedure is performed in an elastic medium for the calculated wavefield potential Φ (from eq. 7) for a central frequency of 8 Hz. The damping applied had to be 10 times stronger than in the acoustic case, with the damping factor at the initial stabilizing iteration equal to the mean amplitude of all recorded pressure signals. All subsequent iterations are carried out with 10% of the initial damping. The obtained results for density (Fig. 15a) and relative density gradients (Fig. 15b) suggest that the structural trends of the true model in the y-direction can be estimated approximately, but contain substantially more artefacts than in the acoustic case (Fig. 6). The sinusoidal trend of the lateral heterogeneity in y-direction is recognisable but its shape is not approximated completely. These distortions are naturally also mapped into estimates of spatial density variations. The poorly constrained results in the x-direction demonstrate relative density gradients deviating from zero, especially between receiver 3 to 6 which does not agree with the constant true model.

By examining the parameter error in x- and y-directions individually it becomes apparent that the parameter error in the x-direction monotonically increases with iterations, whereas the parameter error on the relative gradient in y-direction at first steadily decreases until iteration 60 after which it also follows an increasing trend. Consequently, artefacts are mapped into the density result during the inversion process. False structural density features are thus estimated by the inversion which suggests a strong cross-talk with other material parameters. A trade-off with velocity could cause the trend in velocity gradients in the x-direction, thereby distorting density. By mapping a false trend originating from the velocity error into the x-direction gradient, gradients in y-direction might compensate by over or under-estimating the density variation. The inversion being strongly influenced by the velocity response suggests that density has less weight in the elastic medium compared to the acoustic case. This becomes apparent in the misfit function map that explores the phase velocity and density space, displaying trade-offs between parameters in the acoustic and elastic case (Fig. 16).

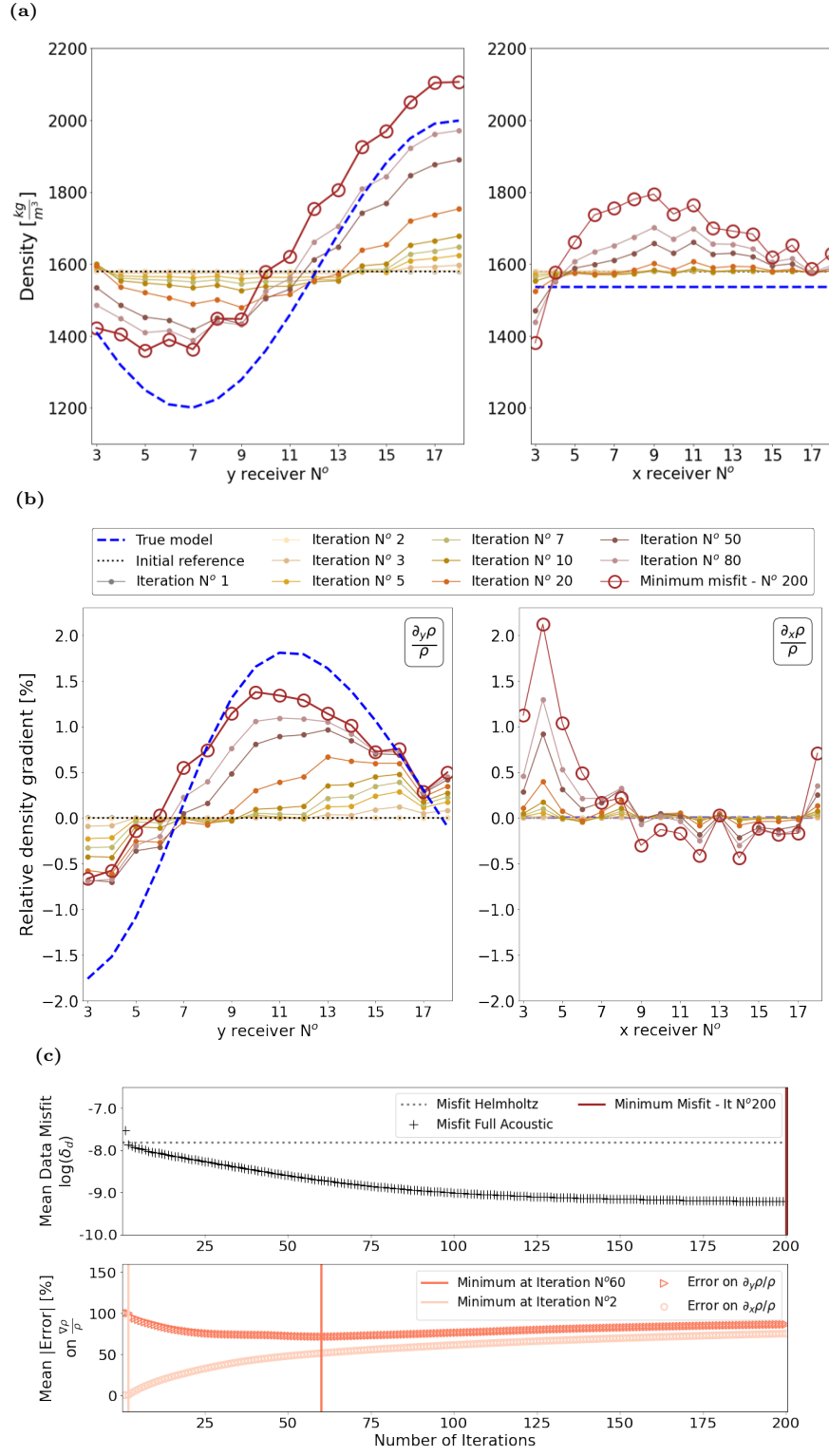


Figure 15: Inversion result for an elastic wavefield filtered to include a frequency range between 7 Hz to 9 Hz. Only the results for the internal receivers 3 to 18 are displayed, as boundary stations need to be disregarded for finite difference estimates and computing pressure entails an additional differentiation step in approximating the divergence of the displacement. Mean value of inverted (a) density and (b) relative density gradient results over all cross-sections in x-plane (left) and y-plane (right) showing the evolution of the inversion at selected points during 200 iterations for a density model with sinusoidal heterogeneity as shown in Fig. 3. True model is depicted as dashed dark blue line and initial model as dotted black line. The minimum misfit result coincides with the last iteration 200 and is highlighted by red circles. (c) Logarithm of the mean data misfit over all internal receivers (upper row) for the full acoustic wave equation (black crosses) over 200 iterations. As a reference, the misfit achieved with linear regression based on the Helmholtz equation is shown by the dotted grey line. Mean parameter error on x- and y- relative gradients is shown in the lower row over all internal receivers. The respective minimum value positions are marked by vertical lines in red for minimum misfit at iteration 200, dark orange and light orange at iteration 60 and 2 for minimum parameter error on relative density gradients in y-direction and x-direction. The minimum mean parameter error is evaluated after the initial stabilizing iteration.

6.1.3 Comparison between acoustic and elastic sensitivities

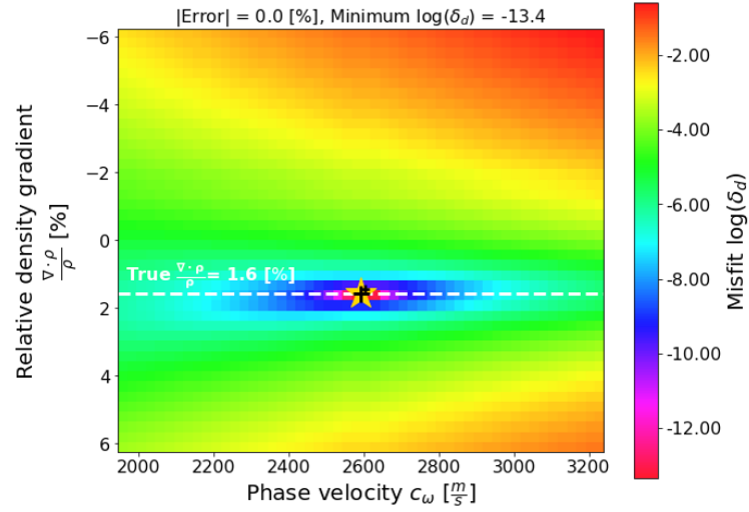
To visualize the sensitivities of the inversion towards the investigated parameters, we perform a grid search where we analyse a grid of potential solutions for phase velocity and relative density gradients, and their misfit to the true model (Eq. 51) at a fixed central receiver location $[x_0, y_0]$ (Fig. 16). The density at the central location is fixed at the true value, but both neighbouring cells in the y-direction are freely variable in order to investigate the misfit evolution for various relative density gradient values. The density at $[y_0 + 1]$ and $[y_0 - 1]$ vary by ± 25 % around the true density value at $[x_0, y_0]$ and produce relative gradient values between ± 6.25 %. The phase velocity at the central point is variable around the phase velocity at $[x_0, y_0]$ obtained by full acoustic WEI and spans a range of ± 25 %.

We compare the misfit function for acoustic and elastic wavefield data at the central frequency of 8 Hz. At the example receiver [13,13], the global misfit minimum is about 3 orders of magnitudes lower in the acoustic case than in the elastic one. This suggests that more uncertainty is attached to the inversion process in the elastic medium given that wavefield traces have been normalised prior to the evaluation.

The misfit function distribution in the acoustic medium shows that density gradients are better constrained than phase velocities (Fig. 16a): for logarithm misfit values within two order of magnitude from the minimum misfit (pink area, $\log(\delta_d) < -11.4$), the phase velocity can vary up to 4% whereas the relative density gradient is better constrained with no fluctuation at all. The absolute minimum misfit coincides exactly with the true value of the relative density gradient ($|\text{Error}| = 0\%$) and the minimum misfit phase velocity agrees well with the reference value of 2570m/s. All iterations from the inversion process plot very closely to the global misfit due to the strong constraints on both parameters.

In elastic media, Figure 16(b) shows that a comparatively large number of relative density gradient and phase velocity values can explain the data on the basis of the full acoustic equation. For all solution pairs with misfit values within two orders of magnitude from the minimum misfit (pink to blue area on Fig. 16(b), $\log(\delta_d) < -8.1$), density gradients vary between 12.8% over the density gradient parameter space, whereas phase velocity fluctuates between 40.8% over the phase velocity parameter space. The comparatively higher uncertainty than in the acoustic case might be attributed to the weaker density signal strength (Fig. 4) and approximations in physics. An error of 12% between the true relative gradient and the global misfit value suggests that the elastic data can not be fully explained by an underlying full acoustic wave equation. This implies that the inversion is prone to converge towards a slightly incorrect relative density gradient value.

(a) Acoustic



(b) Elastic

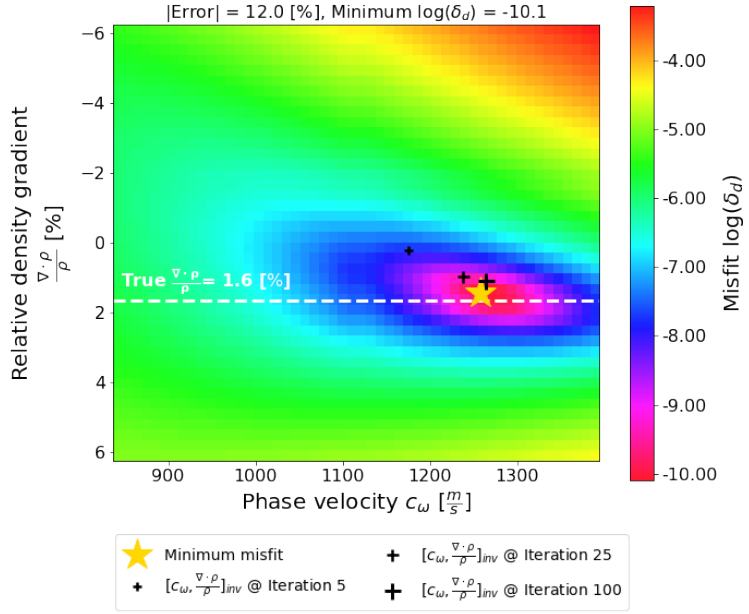


Figure 16: Misfit functions for (a) acoustic and (b) elastic media at receiver location [13,13] for a central frequency of 8 Hz. The misfit function are representative of the data used to produce Figs 6 and 15 respectively. The $|\text{Error}|$ (eq. 52) shows the deviation of the relative density gradient value at the global minimum misfit in the grid search (yellow star) from the true value (white dotted line). Misfit is calculated as defined in eq. (51) and displayed for a single receiver. Crosses of increasing size show how total relative density gradient results of the iterative inversion process converges towards the global misfit of the grid search (small: iteration 5, medium: iteration 25, large: iteration 100).

Iteration 5 of the inversion process gives an estimate on relative density gradient with a misfit value that is far away from the global misfit (about two orders of magnitude) and provides a poor estimate on phase velocity and relative density gradient. Due to the comparatively poor constraints on both parameters, subsequent iterations are subject to parameter cross-talk and artefacts are mapped into the solution, corrupting primarily the relative gradient in the x-direction. Nevertheless, the inversion manages to converge towards a

value in the vicinity of the true relative density gradient. To test the gradiometric estimate on phase velocity at the investigated receiver location, we use the surf-96 code (Herrman, 2013) to calculate an expected value for mean Rayleigh wave velocity between 7 Hz to 9 Hz from the generated dispersion curve. The phase velocity value of 1260m/s corresponding to the lowest misfit marked by the yellow star in Figure 16(b) is only 6% smaller than the expected value of 1340m/s generated by a 2 layer model matching the 1D depth structure at the receiver location in our true model.

In summary, both acoustic and elastic media show sensitivity to relative density gradients. However, relative density gradients might not cause a large enough perturbation in the elastic wavefield to be sufficiently constrained in the inverse problem, whereas in acoustic media they are indeed essential to explain the data.

6.2 Volumetric arrays

6.2.1 Elastic Data

In a first step using a volumetric array, body wave velocities are estimated for a wavefield filtered between 7 Hz to 9 Hz using a least-squares inversion from eq. (18). Those velocity results (Fig. 17a) are substituted into equations (43) to (44) along with the calculated pressure. Pressure at the free surface is given in eq. (11), but we find that using only the related acoustic expression $P = K_a \nabla_H \cdot \mathbf{u}^H$ delivers more reasonable inversion results for density. Figure 17 shows the estimated density results obtained by linear regression of eq. (45). The accuracy of the density results depends on how well the velocities can be estimated. The mean value of the absolute parameter error over the receiver grid (Fig. 17b, right) measures 3.04 % illustrating that the estimated results are close to the true parameter values. Once body wave velocities and densities are estimated, we can proceed to calculate Lamé parameters via empirical relationships: results are shown for the first Lamé parameter in Fig. 17(c).

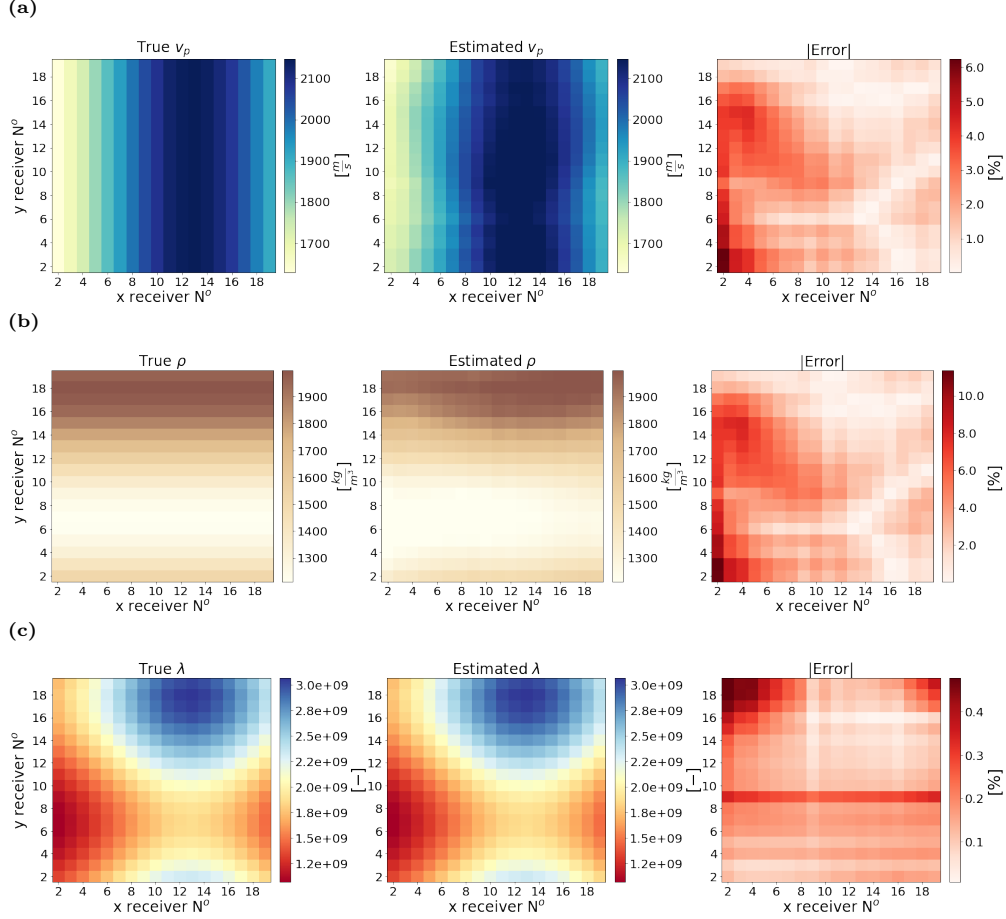


Figure 17: Plan view of (left column) true model and (middle column) gradiometric estimates of material parameters. The corresponding parameter error (Eq. 52) is shown in the right column. Rows (a), (b) and (c) correspond to results for P wave velocity, density and the first Lamé parameter λ . Velocities are estimated via WEI of eq. 18, densities by linear regression of eq. (45) and Lamé parameters are obtained from the latter estimated velocity and density results where $\lambda = (v_P^2 - 2v_S^2)\rho$.

7 Discussion

We have shown that in acoustic media, relative density gradients of 1.6% produce a substantial change in the synthetic wavefield. This allows us to set up an inverse problem that successfully estimates density structure of the medium. Density contrasts down to the amplitude of 0.5% can be imaged with a parameter error smaller than 10% (Figure 7). First tests suggest that the inversion process is robust for random noise up to 1% of the mean trace amplitude (Fig. 14) which encourages a future trial on real data.

In elastic media, other effects interfere with the density signal, making density estimation more difficult from surface array data alone. Elastic results (Section 6.1.2) and sensitivity analysis (Section 6.1.3) show that there is sensitivity to relative density gradients in elastic media. However, the full acoustic approximation

is too severe for elastic wave physics and density is too weakly constrained to be fully estimated using the proposed iterative inversion process. This makes it unlikely that density inversion based on gradiometric full-acoustic WEI will be feasible in an elastic Earth, or worse a visco-elastic Earth where the already small density signal might be overshadowed by the additional medium parameter of energy dissipation. The method might only be applicable in localized areas where the wavefield passes predominantly through gas or liquids.

To estimate density in elastic media it is therefore necessary to use volumetric array measurements and to adopt a more accurate representation of underlying wave physics as a basis for gradiometric WEI, such as the full elastic wave equation. However, it became clear from equation (3a) that if we only measure particle velocity or displacement and if the source term \mathbf{f} is omitted, density does not appear as an independent term outside of the expressions for body wave velocity. It is therefore impossible to estimate density independently of the Lamé parameters using a sourceless full elastic equation. However, if both displacement and pressure are measured in a dual sensor configuration, the full elastic wave equation at the free surface exhibits a direct, independent sensitivity to density in the form of a linear relationship between pressure and displacement terms (Section 6.2). If we are willing to deploy buried receivers then the results herein suggest that density can be estimated directly from recorded data, together with P and S velocities. Pressure sensors for solid earth applications have been presented as a prototype (Edme et al., 2018), but reliable pressure measurements are not readily available as of yet.

While our focus herein has been to make use of the ambient wavefield, an alternative exists if we consider the introduction of a local source within the receiver array. In that case, if the associated body force term \mathbf{f} is clearly defined, density can be isolated within the wave equation and could in theory be estimated. We therefore propose a thought experiment in which we consider a weight drop within a 3D gradiometric receiver array (Fig. 1a) and perform volumetric gradiometry. If we assume that the weight drop acts as a vertical point load on the surface then the body force \mathbf{f} is generally defined as a distribution of force density as a function of position and time (Madariaga, 2007):

$$\mathbf{f}(\mathbf{x}, t) = \mathbf{f}_0 s(t) \delta(\mathbf{x} - \mathbf{x}_0) \quad (53)$$

where \mathbf{f}_0 is a unit vector in the direction of the point force $\mathbf{f}_0 = [0, 0, 1]^T$, $s(t)$ is a source time function (the variation of the amplitude of the force as a function of time) applied in the vertical direction and $\delta(\mathbf{x} - \mathbf{x}_0)$ is the Dirac distribution centered at the source location \mathbf{x}_0 . Neitzel (1958) first analysed the seismic

characteristics of a weight-drop source in a field experiment: he measured the force applied to the ground in an effort to characterise the source term and recorded the wavefield response. Several authors thereafter proposed source term expressions to explain wavefield observations produced by a weight drop: based on the work of Lamb (1904), Pekeris (1955) and Mooney (1974) derived analytical expressions of the wavefield response at the free surface due to the application of an arbitrary excitation. The use of Heaviside step function and Dirac Delta function could not reproduce wavefield quantities accurately, whereas a sinusoidal source time function was shown to better approximate the generated wavefield (Abe et al., 1990). Defining a generalised source term as accurately as possible is an essential task in predicting the Earth response to a weight drop, and hence also in the proposed application to gradiometry. Colombero et al. (2015) found that the source time function in the near-field of a weight drop can be represented by a modified Gabor wavelet (based on Semblat and Pecker (2009)) expressed in terms of particle velocity:

$$s(t) = \begin{cases} C_b \beta t^\gamma \exp[-(\frac{2\pi}{T_s} t)^2] \cos(\frac{2\pi}{T_s} t) & \text{if } 0 \leq t \leq 1.2T_s \\ 0 & \text{otherwise} \end{cases} \quad (54)$$

where t is a generic time instant, T_s the period of the function, C_b the momentum of the dropped weight and α , β and γ are constants whose corresponding values are given in Colombero et al. (2015). By comparing recorded particle velocity from drop load tests and synthetic data generated by propagating the proposed source signal, they found that simulated and real impulse responses in the near-field of the source match well.

We therefore propose that in the case where we allow ourselves the luxury of a local source, the modified Gabor source time wavelet (eq. 54) could in principle be incorporated in the volumetric gradiometry workflow in order to estimate density on the basis of the full elastic wave equation at the free surface. In a first step we consider equation (3a) without body forces. We can then estimate P-wave velocity $v_{P,e}$ and S-wave velocity $v_{S,e}$ at the free surface for any incoming wavefield using volumetric gradiometric measurements and the Lax-Wendroff correction (Lax and Wendroff, 1964) as proposed by Curtis and Robertsson (2002). Then by applying body forces in the form of a weight drop where $s(t)$ is clearly defined (eq. 54), equation (18) that describes the vertical component of a wavefield $\vartheta = [\vartheta_x, \vartheta_y, \vartheta_z]$ at the free surface takes the form:

$$[\partial_t^2 \vartheta_z - v_{P,e}^2 A_z(t) + v_{S,e}^2 B_z(t)] \rho = f \quad (55)$$

with $A_z(t)$ and $B_z(t)$ given in equations (19) to (20). The entire left-hand side of equation (55) is then known apart from density, and takes the form of a linear inverse problem which might be solved for density.

884

885 Theoretically the response at the buried receiver could be inferred analytically by Green’s function retrieval,
 886 if the effective volume encompassed by the gradiometric 3D receiver array is considered a uniform half-space
 887 in accordance with Lamb’s problem. Johnson (1974) and Chen and Cao (2020) provide an expression of the
 888 Green’s function at a buried receiver for a surface source over a homogeneous half-space. By extending this
 889 work to a Gabor wavelet source time function, the wavefield response at a buried receiver could be written
 890 analytically, reducing the acquisition requirements to a surface array.

891 8 Conclusion

892 We investigated whether surface wavefield gradiometry can be used to gain insights into material density
 893 via WEI of the full acoustic wave equation in both 3D acoustic as well as 3D elastic media using ambient
 894 noise data. We propose and test an iterative inversion scheme for both density and phase velocity based on
 895 gradiometric WEI and simulated ambient noise. No inherent scaling between velocity and density is imposed,
 896 making it suitable to detect density changes caused by temperature or chemically induced mechanisms. Syn-
 897 thetic results for 3D acoustic media suggest that it is possible to estimate relative density structure with
 898 WEI by using a full acoustic formulation for wave propagation along the surface. We show that using a
 899 constant density assumption for the medium can be detrimental to subsurface velocity images, whereas the
 900 full acoustic formulation of gradiometry improves our knowledge of all material properties. It allows us
 901 to estimate density as an additional material parameter as well as to improve phase velocity estimates by
 902 incorporating approximations of the density structure.

903

904 By expanding this methodology to the elastic case, we tested the feasibility of estimating density in the solid
 905 Earth with gradiometric WEI on the basis of a full acoustic approximation. The dilatational component of
 906 Rayleigh waves at the free surface was shown to be imprinted by effects from relative density changes in the
 907 medium. It proved however to be more difficult to obtain reliable estimates on relative density changes in
 908 elastic media than in acoustic media due to a stronger trade-off between density and phase velocity caused
 909 by the difference in the measured wave type sensitivities to material parameters in both analysed media.
 910 However, using a 3D array and the full elastic wave equation at the free surface it is possible to obtain reliable
 911 density estimates in elastic media. We suggest that another reasonable way to obtain density estimates in
 912 elastic media would be to fire a local source and include the corresponding source term within an inversion
 913 of the full elastic wave equation.

Acknowledgements

The present project was supported by the National Research Fund (FNR) of Luxembourg and by a Doctoral Training Partnership grant (NE/S007407/1) from the UK Natural Environment Research Council (NERC).

Data Availability

All code and synthetic data used in this study can be shared with any interested party on request to the corresponding author.

References

- Abe, S., Kobayashi, Y., & Ikawa, T. (1990). Seismic characteristics of the weight-dropping source. *Journal of Physics of the Earth*, 38(3), 189–212.
- Afanasiev, M., Boehm, C., van Driel, M., Krischer, L., Rietmann, M., May, D. A., Knepley, M. G., & Fichtner, A. (2019). Modular and flexible spectral-element waveform modelling in two and three dimensions. *Geophysical Journal International*, 216(3), 1675–1692.
- Aki, K., & Richards, P. G. (2002). *Quantitative seismology*. Amundsen, L., Røsten, T., Robertsson, J. O., & Kragh, E. (2005). Rough-sea deghosting of streamer seismic data using pressure gradient approximations. *Geophysics*, 70(1), V1–V9.
- Anderson, S. P., von Blanckenburg, F., & White, A. F. (2007). Physical and chemical controls on the critical zone. *Elements*, 3(5), 315–319.
- Befus, K., Sheehan, A., Leopold, M., Anderson, S., & Anderson, R. (2011). Seismic constraints on critical zone architecture, boulder creek watershed. *Vadose Zone Journal*, 10(3), 915–927.
- Bergmann, P. G. (1946). The wave equation in a medium with a variable index of refraction. *The Journal of the Acoustical Society of America*, 17(4), 329–333.
- Blanch, J., & Robertsson, J. O. (1997). A modified lax-wendroff correction for wave propagation in media described by zener elements. *Geophysical Journal International*, 131(2), 381–386.
- Blom, N., Boehm, C., & Fichtner, A. (2017). Synthetic inversions for density using seismic and gravity data. *Geophysical Journal International*, 209(2), 1204–1220.
- Blom, N., Gokhberg, A., & Fichtner, A. (2020). Seismic waveform tomography of the central and eastern mediterranean upper mantle. *Solid Earth*, 11(2), 669–690.
- Boddice, D., Metje, N., & Tuckwell, G. (2019). Quantifying the effects of near surface density variation on quantum technology gravity and gravity gradient instruments. *Journal of Applied Geophysics*, 164, 160–178.
- Boddice, D., Metje, N., & Tuckwell, G. (2022). Microgravity surveying before, during and after distant large earthquakes. *Journal of Applied Geophysics*, 197, 104542.
- Brimhall, G. H., Chadwick, O. A., Lewis, C. J., Compston, W., Williams, I. S., Danti, K. J., Dietrich, W. E., Power, M. E., Hendricks, D., & Bratt, J. (1992). Deformational mass transport and invasive processes in soil evolution. *Science*, 255(5045), 695–702.
- Cance, P., & Capdeville, Y. (2015). Validity of the acoustic approximation for elastic waves in heterogeneous media: a cooustic approximation of elastic waves. *Geophysics*, 80(4), T161–T173.
- Cao, R., Earp, S., de Ridder, S. A., Curtis, A., & Galetti, E. (2020). Near-real-time near-surface 3d seismic velocity and uncertainty models by wavefield gradiometry and neural network inversion of ambient seismic noise. *Geophysics*, 85(1), KS13–KS27.
- Chen, J.-B., & Cao, J. (2020). Green’s function for three-dimensional elastic wave equation with a moving point source on the free surface with applications. *Geophysical Prospecting*, 68(4), 1281–1290.
- Choi, Y., Min, D.-J., & Shin, C. (2008). Frequency-domain elastic full waveform inversion using the new pseudo-hessian matrix: Experience of elastic marmousi-2 synthetic data. *Bulletin of the Seismological Society of America*, 98(5), 2402–2415.
- Colombero, R., Kontoe, S., Foti, S., & Potts, D. (2015). Numerical modelling of drop load tests. *Soil Dynamics and Earthquake Engineering*, 77, 279–289.
- Curtis, A., Gerstoft, P., Sato, H., Snieder, R., & Wapenaar, K. (2006). Seismic interferometry—turning noise into signal. *The Leading Edge*, 25(9), 1082–1092.
- Curtis, A., & Robertsson, J. O. (2002). Volumetric wavefield recording and wave equation inversion for near-surface material properties. *Geophysics*, 67(5), 1602–1611.
- De Ridder, S., & Biondi, B. (2015). Near-surface scholte wave velocities at ekofisk from short noise recordings by seismic noise gradiometry. *Geophysical Research Letters*, 42(17), 7031–7038.
- De Ridder, S., & Curtis, A. (2017). Seismic gradiometry using ambient seismic noise in an anisotropic earth. *Geophysical Journal International*, 209(2), 1168–1179.
- Dexter, A. (2004). Soil physical quality: Part i. theory, effects of soil texture, density, and organic matter, and effects on root growth. *Geoderma*, 120(3–4), 201–214.
- Edme, P., Muzyert, E., Goujon, N., El Allouche, N., & Kragh, E. (2018). Seismic wavefield divergence at the free surface. *First Break*, 36(12), 75–82.
- Edme, P., & Yuan, S. (2016). Local dispersion curve estimation from seismic ambient noise using spatial gradients. *Interpretation*, 4(3), SJ17–SJ27.
- Fanchi, J. R. (2010). 7 - well logging. In J. R. Fanchi (Ed.), *Integrated reservoir asset management* (pp. 109–124). Gulf Professional Publishing. <https://doi.org/https://doi.org/10.1016/B978-0-12-382088-4.00007-4>
- Fichtner, A. (2010). *Full seismic waveform modelling and inversion*. Springer Science & Business Media.
- Flinchum, B. A., Holbrook, W. S., & Carr, B. J. (2022). What do p-wave velocities tell us about the critical zone? *Frontiers in Water*, 3, 772185.
- Flinchum, B. A., Holbrook, W. S., Grana, D., Parsekian, A. D., Carr, B. J., Hayes, J. L., & Jiao, J. (2018). Estimating the water holding capacity of the critical zone using near-surface geophysics. *Hydrological Processes*, 32(22), 3308–3326.
- Foti, S., Hollender, F., Garofalo, F., Albarello, D., Asten, M., Bard, P.-Y., Comina, C., Cornou, C., Cox, B., Di Giulio, G., et al. (2018). Guidelines for the good practice of surface wave analysis: A product of the intercalibration project. *Bulletin of Earthquake Engineering*, 16, 2367–2420.
- Friederich, W., Hunzinger, S., & Wielandt, E. (2000). A note on the interpretation of seismic surface waves over three - dimensional structures. *Geophysical Journal International*, 143(2), 335–339. <https://doi.org/10.1046/j.1365-246X.2000.01241.x>
- Gardner, G., Gardner, L., & Gregory, A. (1974). Formation velocity and density—the diagnostic basics for stratigraphic traps. *Geophysics*, 39(6), 770–780.
- Gavete, L., Gavete, M., & Benito, J. (2003). Improvements of generalized finite difference method and comparison with other meshless method. *Applied Mathematical Modelling*, 27(10), 831–847.
- Geiger, H. D., & Daley, P. F. (2003). Finite difference modelling of the full acoustic wave equation in matlab.
- Handoyo, H., Alcalde, J., DeFelipe, I., Palomeras, I., Martín-Banda, R., García-Mayordomo, J., Martí, D., Martínez-Díaz, J. J., Insua-Arévalo, J. M., Teixidó, T., et al. (2022). Geophysical imaging of the critical zone along the eastern betic shear zone (ebsz), se iberian peninsula. *Applied Sciences*, 12(7), 3398.

- Herrman, R. (2013). Computer programs in seismology: An evolving tool for instructijn and researcher.(2003) *seism. Res. Let.*, 84(6), 1081–1088.
- Holbrook, W. S., Marcon, V., Bacon, A. R., Brantley, S. L., Carr, B. J., Flinchum, B. A., Richter, D. D., & Riebe, C. S. (2019). Links between physical and chemical weathering inferred from a 65-m-deep borehole through earth's critical zone. *Scientific Reports*, 9(1), 4495.
- Holbrook, W. S., Riebe, C. S., Elwaseif, M., L. Hayes, J., Basler-Reeder, K., L. Harry, D., Malazian, A., Dosseto, A., C. Hartsough, P., & W. Hopmans, J. (2014). Geophysical constraints on deep weathering and water storage potential in the southern sierra critical zone observatory. *Earth Surface Processes and Landforms*, 39(3), 366–380.
- Huang, C., Shao, M., & Tan, W. (2011). Soil shrinkage and hydrostructural characteristics of three swelling soils in shaanxi, china. *Journal of Soils and Sediments*, 11, 474–481.
- Huiskamp, G. (1991). Difference formulas for the surface laplacian on a triangulated surface. *Journal of computational physics*, 95(2), 477–496.
- Ivanov, J., Tsoflias, G., Miller, R. D., Peterie, S., Morton, S., & Xia, J. (2016). Impact of density information on rayleigh surface wave inversion results. *Journal of Applied Geophysics*, 135, 43–54.
- James, S., Knox, H., Abbott, R., Panning, M., & Screaton, E. (2019). Insights into permafrost and seasonal active-layer dynamics from ambient seismic noise monitoring. *Journal of Geophysical Research: Earth Surface*, 124(7), 1798–1816.
- Jeong, W., Lee, H.-Y., & Min, D.-J. (2012). Full waveform inversion strategy for density in the frequency domain. *Geophysical Journal International*, 188(3), 1221–1242.
- Johnson, L. R. (1974). Green's function for lamb's problem. *Geophysical Journal International*, 37(1), 99–131.
- Karato, S.-i., & Karki, B. B. (2001). Origin of lateral variation of seismic wave velocities and density in the deep mantle. *Journal of Geophysical Research: Solid Earth*, 106(B10), 21771–21783.
- Kaufman, A. A., Levshin, A. L., & Lerner, K. L. (2000). *Acoustic and elastic wave fields in geophysics* (Vol. 2). Gulf Professional Publishing.
- Köhn, D., De Nil, D., Kurzmann, A., Przebindowska, A., & Bohlen, T. (2012). On the influence of model parametrization in elastic full waveform tomography. *Geophysical Journal International*, 191(1), 325–345.
- Lamb, H. (1904). I. on the propagation of tremors over the surface of an elastic solid. *Philosophical Transactions of the Royal Society of London. Series A, Containing papers of a mathematical or physical character*, 203(359-371), 1–42.
- Langston, C. A. (2007a). Wave gradiometry in the time domain. *Bulletin of the Seismological Society of America*, 97(3), 926–933. <https://doi.org/10.1785/0120060152>
- Langston, C. A. (2007b). Spatial gradient analysis for linear seismic arrays. *Bulletin of the Seismological Society of America*, 97(1B), 265–280. <https://doi.org/10.1785/0120060100>
- Langston, C. A. (2007c). Wave gradiometry in two dimensions. *Bulletin of the Seismological Society of America*, 97(2), 401–416. <https://doi.org/10.1785/0120060138>
- Lax, P. D., & Wendroff, B. (1964). Difference schemes for hyperbolic equations with high order of accuracy. *Communications on pure and applied mathematics*, 17(3), 381–398.
- Liang, C., Cao, F., Liu, Z., & Chang, Y. (2023). A review of the wave gradiometry method for seismic imaging. *Earthquake Science*, 36(3), 254–281.
- Liang, C., & Langston, C. A. (2009). Wave gradiometry for usarray: Rayleigh waves. *Journal of Geophysical Research: Solid Earth*, 114(B2).
- Lin, F.-C., Tsai, V. C., & Ritzwoller, M. H. (2012). The local amplification of surface waves: A new observable to constrain elastic velocities, density, and anelastic attenuation. *Journal of Geophysical Research: Solid Earth*, 117(B6).
- Liszka, T., & Orkisz, J. (1980). The finite difference method at arbitrary irregular grids and its application in applied mechanics. *Computers & Structures*, 11(1-2), 83–95.
- Liu, Y., & Holt, W. E. (2015). Wave gradiometry and its link with helmholtz equation solutions applied to usarray in the eastern us. *Journal of Geophysical Research: Solid Earth*, 120(8), 5717–5746.
- Luo, J., & Wu, R.-S. (2018). Velocity and density reconstruction based on scattering angle separation. *Pure and Applied Geophysics*, 175, 4371–4387.
- Madariaga, R. (2007). Seismic source theory. *Earthquake seismology*, 4, 59–82.
- Maeda, T., Nishida, K., Takagi, R., & Obara, K. (2016). Reconstruction of a 2d seismic wavefield by seismic gradiometry. *Progress in Earth and Planetary Science*, 3(1), 1–17.
- Mooney, H. M. (1974). Some numerical solutions for lamb's problem. *Bulletin of the Seismological Society of America*, 64(2), 473–491.
- Mosca, I., Cobden, L., Deuss, A., Ritsema, J., & Trampert, J. (2012). Seismic and mineralogical structures of the lower mantle from probabilistic tomography. *Journal of Geophysical Research: Solid Earth*, 117(B6).
- Muijs, R., Holliger, K., & Robertsson, J. O. (2002). Perturbation analysis of an explicit wavefield separation scheme for p-and s-waves. *Geophysics*, 67(6), 1972–1982.
- Muyzert, E., & Snieder, R. (2000). An alternative parameterisation for surface waves in a transverse isotropic medium. *Physics of the Earth and Planetary Interiors*, 118(1-2), 125–133.
- Nabighian, M. N., Ander, M., Grauch, V., Hansen, R., LaFehr, T., Li, Y., Pearson, W., Peirce, J., Phillips, J., & Ruder, M. (2005). Historical development of the gravity method in exploration/historical development of gravity method. *Geophysics*, 70(6), 63ND–89ND.
- Nakata, N., Gualtieri, L., & Fichtner, A. (2019). *Seismic ambient noise*. Cambridge University Press.
- Nanko, K., Ugawa, S., Hashimoto, S., Imaaya, A., Kobayashi, M., Sakai, H., Ishizuka, S., Miura, S., Tanaka, N., Takahashi, M., et al. (2014). A pedotransfer function for estimating bulk density of forest soil in japan affected by volcanic ash. *Geoderma*, 213, 36–45.
- Neitzel, E. B. (1958). Seismic reflection records obtained by dropping a weight. *Geophysics*, 23(1), 58–80.
- Nielson, T., Bradford, J., Holbrook, W. S., & Seyfried, M. (2021). The effect of aspect and elevation on critical zone architecture in the reynolds creek critical zone observatory: A seismic refraction study. *Frontiers in Water*, 3, 670524.
- Nolet, G., et al. (1977). The upper mantle under western europe inferred from the dispersion of rayleigh modes. *Journal of Geophysics*, 43(1), 265–285.
- Oakley, D. O., Forsythe, B., Gu, X., Nyblade, A. A., & Brantley, S. L. (2021). Seismic ambient noise analyses reveal changing temperature and water signals to 10s of meters depth in the critical zone. *Journal of Geophysical Research: Earth Surface*, 126(2), e2020JF005823.
- Obermann, A., Kraft, T., Larose, E., & Wiemer, S. (2015). Potential of ambient seismic noise techniques to monitor the st. gallen geothermal site (switzerland). *Journal of Geophysical Research: Solid Earth*, 120(6), 4301–4316.

- Operto, S., & Miniussi, A. (2018). On the role of density and attenuation in three-dimensional multiparameter viscoacoustic VTI frequency-domain FWI: an OBC case study from the North Sea. *Geophysical Journal International*, 213(3), 2037–2059. <https://doi.org/10.1093/gji/ggy103>
- Pan, L., Chen, X., Wang, J., Yang, Z., & Zhang, D. (2019). Sensitivity analysis of dispersion curves of rayleigh waves with fundamental and higher modes. *Geophysical Journal International*, 216(2), 1276–1303.
- Pan, W., Geng, Y., & Innanen, K. A. (2018). Interparameter trade-off quantification and reduction in isotropic-elastic full-waveform inversion: Synthetic experiments and hussar land data set application. *Geophysical Journal International*, 213(2), 1305–1333.
- Parsekian, A., Singha, K., Minsley, B. J., Holbrook, W. S., & Slater, L. (2015). Multiscale geophysical imaging of the critical zone. *Reviews of Geophysics*, 53(1), 1–26.
- Pekeris, C. (1955). The seismic surface pulse. *Proceedings of the national academy of sciences*, 41(7), 469–480.
- Piccolroaz, S., Majone, B., Palmieri, F., Cassiani, G., & Bellin, A. (2015). On the use of spatially distributed, time-lapse microgravity surveys to inform hydrological modeling. *Water Resources Research*, 51(9), 7270–7288.
- Plonka, A., Blom, N., & Fichtner, A. (2016). The imprint of crustal density heterogeneities on regional seismic wave propagation. *Solid Earth*, 7(6), 1591–1608.
- Prieux, V., Brossier, R., Operto, S., & Virieux, J. (2013). Multiparameter full waveform inversion of multicomponent ocean-bottom-cable data from the valhall field. part 1: Imaging compressional wave speed, density and attenuation. *Geophysical Journal International*, 194(3), 1640–1664.
- Qiao, J., Zhu, Y., Jia, X., Huang, L., & Shao, M. (2019). Development of pedotransfer functions for predicting the bulk density in the critical zone on the loess plateau, china. *Journal of soils and sediments*, 19, 366–372.
- Resovsky, J., & Trampert, J. (2003). Using probabilistic seismic tomography to test mantle velocity–density relationships. *Earth and Planetary Science Letters*, 215(1-2), 121–134.
- Riebe, C. S., Hahm, W. J., & Brantley, S. L. (2017). Controls on deep critical zone architecture: A historical review and four testable hypotheses. *Earth Surface Processes and Landforms*, 42(1), 128–156.
- Robertsson, J. O., & Curtis, A. (2002). Wavefield separation using densely deployed three-component single-sensor groups in land surface-seismic recordings. *Geophysics*, 67(5), 1624–1633.
- Robertsson, J. O., & Kragh, E. (2002). Rough-sea deghosting using a single streamer and a pressure gradient approximation. *Geophysics*, 67(6), 2005–2011.
- Robertsson, J. O., & Muzert, E. (1999). Wavefield separation using a volume distribution of three component recordings. *Geophysical Research Letters*, 26(18), 2821–2824.
- Schmelzbach, C., Donner, S., Igel, H., Sollberger, D., Taufiqurrahman, T., Bernauer, F., Häusler, M., Van Renterghem, C., Wassermann, J., & Robertsson, J. (2018). Advances in 6c seismology: Applications of combined translational and rotational motion measurements in global and exploration seismology. *Advances in 6c seismology. Geophysics*, 83(3), WC53–WC69.
- Semblat, J., & Pecker, A. (2009). Waves and vibrations in soils. *Earthquakes, traffic, shocks*, 13.
- Shaiban, A., De Ridder, S., & Curtis, A. (2022). Wavefield reconstruction and wave equation inversion for seismic surface waves. *Geophysical Journal International*, 229(3), 1870–1880.
- Shapiro, N., Campillo, M., Margerin, L., Singh, S., Kostoglodov, V., & Pacheco, J. (2000). The energy partitioning and the diffusive character of the seismic coda. *Bulletin of the Seismological Society of America*, 90(3), 655–665.
- Shearer, P. M. (2019). *Introduction to seismology*. Cambridge university press.
- Sollberger, D., Bradley, N., Edme, P., & Robertsson, J. O. (2023). Efficient wave type fingerprinting and filtering by six-component polarization analysis. *Geophysical Journal International*, 234(1), 25–39.
- Sollberger, D., Igel, H., Schmelzbach, C., Edme, P., Van Manen, D.-J., Bernauer, F., Yuan, S., Wassermann, J., Schreiber, U., & Robertsson, J. O. (2020). Seismological processing of six degree-of-freedom ground-motion data. *Sensors*, 20(23), 6904.
- Sollberger, D., Schmelzbach, C., Robertsson, J. O., Greenhalgh, S. A., Nakamura, Y., & Khan, A. (2016). The shallow elastic structure of the lunar crust: New insights from seismic wavefield gradient analysis. *Geophysical Research Letters*, 43(19), 10–078.
- Suuster, E., Ritz, C., Roostalu, H., Reintam, E., Kölli, R., & Astover, A. (2011). Soil bulk density pedotransfer functions of the humus horizon in arable soils. *Geoderma*, 163(1-2), 74–82.
- Takeuchi, H., & Saito, M. (1972). Seismic surface waves. *Methods in computational physics*, 11, 217–295.
- Tanimoto, T. (1991). Waveform inversion for three-dimensional density and s wave structure. *Journal of Geophysical Research: Solid Earth*, 96(B5), 8167–8189.
- Trampert, J., Deschamps, F., Resovsky, J., & Yuen, D. (2004). Probabilistic tomography maps chemical heterogeneities throughout the lower mantle. *Science*, 306(5697), 853–856.
- Trichandi, R., Bauer, K., Ryberg, T., Scherler, D., Bataille, K., & Krawczyk, C. M. (2022). Combined seismic and borehole investigation of the deep granite weathering structure—santa gracia reserve case in chile. *Earth Surface Processes and Landforms*, 47(14), 3302–3316.
- Tuckwell, G., Grossey, T., Owen, S., & Stearns, P. (2008). The use of microgravity to detect small distributed voids and low-density ground. *Quarterly Journal of Engineering Geology and Hydrogeology*, 41(3), 371–380.
- Vantassel, J. P., Kumar, K., & Cox, B. R. (2022). Using convolutional neural networks to develop starting models for near-surface 2-d full waveform inversion. *Geophysical Journal International*, 231(1), 72–90.
- Virieux, J., & Operto, S. (2009). An overview of full-waveform inversion in exploration geophysics. *Geophysics*, 74(6), WCC1–WCC26.
- Vossen, R. v., Trampert, J., & Curtis, A. (2004). Propagator and wave-equation inversion for near-receiver material properties. *Geophysical Journal International*, 157(2), 796–812.
- Wiandl, E. (1993). Propagation and Structural Interpretation of Non-Plane Waves. *Geophysical Journal International*, 113(1), 45–53. <https://doi.org/10.1111/j.1365-246X.1993.tb02527.x>
- Wu, G.-x., Pan, L., Wang, J.-n., & Chen, X. (2020). Shear velocity inversion using multimodal dispersion curves from ambient seismic noise data of usarray transportable array. *Journal of Geophysical Research: Solid Earth*, 125(1), e2019JB018213.
- Yuan, Y. O., Simons, F. J., & Bozdağ, E. (2015). Multiscale adjoint waveform tomography for surface and body waves. *Geophysics*, 80(5), R281–R302.

Appendix

A Finite Difference Error

Throughout this analysis we use 2nd order accurate formulations of the finite difference approximation of the 2nd spatial derivative of the wavefield quantity ϑ :

$$\frac{\partial^2 \vartheta}{\partial x^2} = \frac{\vartheta(x - \Delta x) - 2\vartheta(x) + \vartheta(x + \Delta x)}{\Delta x^2} - \frac{\Delta x^2}{24} \frac{\partial^4 \vartheta}{\partial x^4} \quad (\text{A1})$$

Following (Langston, 2007b) we can calculate the error of this approximation due to the sampling for a sinusoidal wave by assuming a plane wave in the form

$$\vartheta(x, t) = e^{i\omega(t - \frac{x}{c})} \quad (\text{A2})$$

We can then calculate the error ε based on the following formulation:

$$\varepsilon = \left| \frac{-\frac{1}{24} \frac{\partial^4 \vartheta}{\partial x^4}}{\frac{\partial^2 \vartheta}{\partial x^2}} \right| = \frac{\Delta x^2 (2\pi)^2}{24\lambda^2} \quad (\text{A3})$$

Setting an accuracy threshold ζ for the second derivative, the condition

$$\varepsilon \leq \zeta \Leftrightarrow \Delta x \leq \sqrt{\frac{\zeta 24\lambda^2}{(2\pi)^2}} \quad (\text{A4})$$

implies the spacing Δx needs to be at least 0.247λ to ensure an error lower than $\zeta = 0.1$.

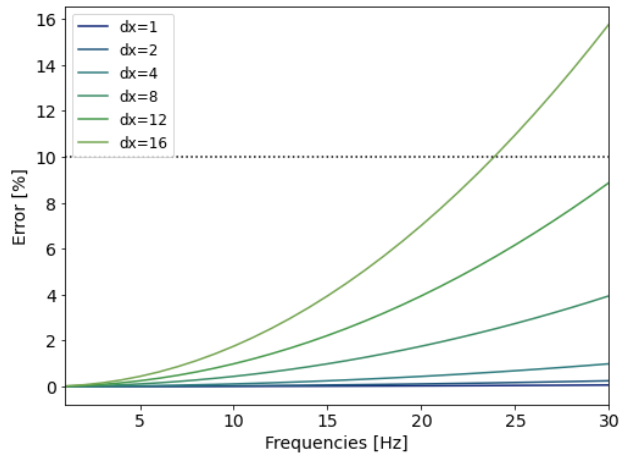


Figure A1: Error evolution of the used Finite Difference approximation with frequency for different receiver spacings given in m. Black dotted line shows threshold error of 10 %.

B Reference Density Model

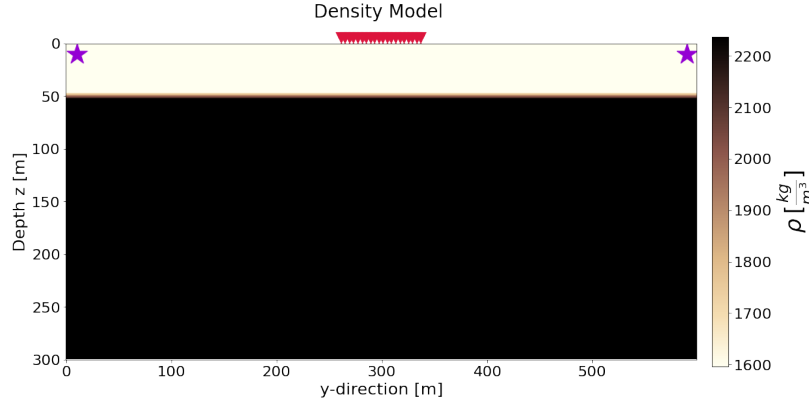


Figure B1: Reference density model depth cross-section in yz-plane. A constant density of 1600 kg/m^3 is used for the top layer instead of the variable density structure imposed in Figure 3c and 3d. 1600 kg/m^3 corresponds to the mean value of the top layer in the variable density model.

C Notes on the free surface methodology in inhomogeneous elastic media

In the body of this manuscript, all derivations from Newton's second law in equation (1) are based on the assumption that Lamé parameters are constant over space (eq. 2a in elastic media and eq. 2b in acoustic media). For laterally varying Lamé parameters, these equations become:

$$\underbrace{\frac{(\lambda + 2\mu)}{\rho} [\nabla(\nabla \cdot \mathbf{u})] - \frac{\mu}{\rho} [\nabla \times (\nabla \times \mathbf{u})]}_{\text{homogeneous terms}} + \underbrace{\frac{\nabla \lambda}{\rho} (\nabla \cdot \mathbf{u}) + \frac{\nabla \mu}{\rho} \cdot [\nabla \mathbf{u} + (\nabla \mathbf{u})^T]}_{\text{inhomogeneous terms}} + \frac{\mathbf{f}}{\rho} = \partial_t^2 \mathbf{u} \quad (\text{C1a})$$

$$\underbrace{\frac{\lambda}{\rho} [\nabla(\nabla \cdot \mathbf{u})]}_{\text{homogeneous terms}} + \underbrace{\frac{\nabla \lambda}{\rho} (\nabla \cdot \mathbf{u})}_{\text{inhomogeneous terms}} + \frac{\mathbf{f}}{\rho} = \partial_t^2 \mathbf{u} \quad (\text{C1b})$$

Here we investigate the effect that inhomogeneity has on the derivation of the equations in the free surface methodology used to estimate density and body wave velocities at the free surface presented in Section (2). Writing (C1a) with all terms:

$$\begin{aligned}
& \underbrace{\frac{(\lambda + 2\mu)}{\rho} \begin{pmatrix} \frac{\partial^2 u_x}{\partial x^2} + \frac{\partial^2 u_y}{\partial x \partial y} + \frac{\partial^2 u_z}{\partial x \partial z} \\ \frac{\partial^2 u_x}{\partial y \partial x} + \frac{\partial^2 u_y}{\partial^2 y} + \frac{\partial^2 u_z}{\partial y \partial z} \\ \frac{\partial^2 u_x}{\partial z \partial x} + \frac{\partial^2 u_y}{\partial z \partial y} + \frac{\partial^2 u_z}{\partial^2 z} \end{pmatrix} - \frac{\mu}{\rho} \begin{pmatrix} \frac{\partial^2 u_y}{\partial y \partial x} - \frac{\partial^2 u_x}{\partial^2 y} - \frac{\partial^2 u_x}{\partial^2 z} + \frac{\partial^2 u_z}{\partial x \partial z} \\ \frac{\partial^2 u_z}{\partial z \partial y} - \frac{\partial^2 u_y}{\partial^2 z} - \frac{\partial^2 u_y}{\partial^2 x} + \frac{\partial^2 u_x}{\partial x \partial y} \\ \frac{\partial^2 u_x}{\partial x \partial z} - \frac{\partial^2 u_z}{\partial^2 x} - \frac{\partial^2 u_z}{\partial^2 y} + \frac{\partial^2 u_y}{\partial y \partial z} \end{pmatrix}}_{\text{homogeneous terms}} \\
& + \underbrace{\frac{1}{\rho} \begin{pmatrix} \frac{\partial \lambda}{\partial x} \\ \frac{\partial \lambda}{\partial y} \\ \frac{\partial \lambda}{\partial z} \end{pmatrix} \left(\frac{\partial u_x}{\partial x} + \frac{\partial u_y}{\partial y} + \frac{\partial u_z}{\partial z} \right) + \frac{1}{\rho} \begin{pmatrix} \frac{\partial \mu}{\partial x} \\ \frac{\partial \mu}{\partial y} \\ \frac{\partial \mu}{\partial z} \end{pmatrix} \cdot \left[\begin{pmatrix} \frac{\partial u_x}{\partial x} & \frac{\partial u_x}{\partial y} & \frac{\partial u_x}{\partial z} \\ \frac{\partial u_y}{\partial x} & \frac{\partial u_y}{\partial y} & \frac{\partial u_y}{\partial z} \\ \frac{\partial u_z}{\partial x} & \frac{\partial u_z}{\partial y} & \frac{\partial u_z}{\partial z} \end{pmatrix} + \begin{pmatrix} \frac{\partial u_x}{\partial x} & \frac{\partial u_y}{\partial x} & \frac{\partial u_z}{\partial x} \\ \frac{\partial u_x}{\partial y} & \frac{\partial u_y}{\partial y} & \frac{\partial u_z}{\partial y} \\ \frac{\partial u_x}{\partial z} & \frac{\partial u_y}{\partial z} & \frac{\partial u_z}{\partial z} \end{pmatrix} \right]}_{\text{inhomogeneous terms}} \\
& = \begin{pmatrix} \frac{\partial^2 u_x}{\partial t^2} \\ \frac{\partial^2 u_y}{\partial t^2} \\ \frac{\partial^2 u_z}{\partial t^2} \end{pmatrix} - \frac{1}{\rho} \begin{pmatrix} f_x \\ f_y \\ f_z \end{pmatrix}
\end{aligned} \tag{C2}$$

1334 we can use the free surface conditions

$$\frac{\partial u_z}{\partial z} = -\frac{v_p^2 - 2v_s^2}{v_p^2} \left(\frac{\partial u_x}{\partial x} + \frac{\partial u_y}{\partial y} \right) \tag{C3}$$

$$\frac{\partial u_y}{\partial z} = -\frac{\partial u_z}{\partial y} \tag{C4}$$

$$\frac{\partial u_x}{\partial z} = -\frac{\partial u_z}{\partial x} \tag{C5}$$

1335 to derive the corresponding expression at the free surface. The expression of the homogeneous terms are
1336 described in (Curtis and Robertsson, 2002) and the inhomogeneous terms become:

- 1337 • Term 3 of eq.(C3)

$$\frac{1}{\rho} \begin{pmatrix} \frac{\partial \lambda}{\partial x} \\ \frac{\partial \lambda}{\partial y} \\ \frac{\partial \lambda}{\partial z} \end{pmatrix} \left(\frac{\partial u_x}{\partial x} + \frac{\partial u_y}{\partial y} - \frac{v_p^2 - 2v_s^2}{v_p^2} (\nabla^H \cdot \mathbf{u}_H) \right) \tag{C6}$$

- Term 4 of eq.(C3)

$$\frac{1}{\rho} \begin{pmatrix} \frac{\partial \mu}{\partial x} \\ \frac{\partial \mu}{\partial y} \\ \frac{\partial \mu}{\partial z} \end{pmatrix} \cdot \begin{pmatrix} \frac{2\partial u_x}{\partial x} & \frac{\partial u_x}{\partial y} + \frac{\partial u_y}{\partial x} & \frac{\partial u_x}{\partial z} + \frac{\partial u_z}{\partial x} \\ \frac{\partial u_y}{\partial x} + \frac{\partial u_x}{\partial y} & 2\frac{\partial u_y}{\partial y} & \frac{\partial u_y}{\partial z} + \frac{\partial u_z}{\partial y} \\ \frac{\partial u_z}{\partial x} + \frac{\partial u_x}{\partial z} & \frac{\partial u_z}{\partial y} + \frac{\partial u_y}{\partial z} & 2\frac{\partial u_z}{\partial z} \end{pmatrix} \quad (C7)$$

$$= \frac{1}{\rho} \begin{pmatrix} \frac{\partial \mu}{\partial x} \\ \frac{\partial \mu}{\partial y} \\ \frac{\partial \mu}{\partial z} \end{pmatrix} \cdot \begin{pmatrix} \frac{2\partial u_x}{\partial x} & \frac{\partial u_x}{\partial y} + \frac{\partial u_y}{\partial x} & -\frac{\partial u_z}{\partial x} + \frac{\partial u_z}{\partial x} \\ \frac{\partial u_y}{\partial x} + \frac{\partial u_x}{\partial y} & 2\frac{\partial u_y}{\partial y} & -\frac{\partial u_z}{\partial y} + \frac{\partial u_z}{\partial y} \\ \frac{\partial u_z}{\partial x} - \frac{\partial u_z}{\partial x} & \frac{\partial u_z}{\partial y} - \frac{\partial u_z}{\partial y} & -2\frac{v_p^2 - 2v_s^2}{v_p^2} \nabla^H \cdot \mathbf{u}_H \end{pmatrix} \quad (C8)$$

$$= \frac{1}{\rho} \begin{pmatrix} [\frac{\partial \mu}{\partial x} (\frac{2\partial u_x}{\partial x})] + [\frac{\partial \mu}{\partial y} (\frac{\partial u_x}{\partial y} + \frac{\partial u_y}{\partial x})] + 0 \\ [\frac{\partial \mu}{\partial x} (\frac{\partial u_y}{\partial x} + \frac{\partial u_x}{\partial y})] + [\frac{\partial \mu}{\partial y} (2\frac{\partial u_y}{\partial y})] + 0 \\ 0 + 0 + [\frac{\partial \mu}{\partial z} (-2\frac{v_p^2 - 2v_s^2}{v_p^2} \nabla^H \cdot \mathbf{u}_H)] \end{pmatrix} \quad (C9)$$

1339 In our model, the receiver is buried at 1 m and the Lamé parameters do not change over the depth interval
 1340 used for the calculation of the finite difference approximation of the first order depth derivative. We can
 1341 thus consider the depth derivatives of Lamé parameters $\partial\mu/\partial z$ and $\partial\lambda/\partial z$ to be zero, and the inhomogeneous
 1342 terms disappear in the vertical component of the full elastic wave equation at the free surface.